Naval Information Warfare Center PACIFIC

TECHNICAL REPORT 3253
November 2021

UAV Urban Channels Part I: Bottom-Mounted Whip at 500 MHz

Michael Daly
Jeffery Allen
John Meloling

NIWC Pacific

Naval Information Warfare Center Pacific (NIWC Pacific)
San Diego, CA 92152-5001

This page is intentionally blank.

TECHNICAL REPORT 3253
November 2021

UAV Urban Channels Part I: Bottom-Mounted Whip at 500 MHz

Michael Daly
Jeffery Allen
John Meloling

NIWC Pacific

Administrative Notes:
This report was approved through the Release of Scientific and Technical Information (RSTI) process in May 2018 and formally published in the Defense Technical Information Center (DTIC) in November 2021.

NIWC Pacific
San Diego, CA 92152-5001

NIWC Pacific
San Diego, California 92152-5001

A. D. Gainer, CAPT, USN
Commanding Officer

W. R. Bonwit
Executive Director

ADMINISTRATIVE INFORMATION

The work described in this report was performed by the Applied Electromagnetics Branch of the Electromagnetics and Advanced Technology Division, Naval Information Warfare Center Pacific (NIWC Pacific), San Diego, CA.

Released by
Jodi B. Mcgee, Division Head
Electromagnetics and Advanced Technology Division

Under authority of
Carly Jackson, Department Head
Cyber/S&T Department

Editor: RJP

EXECUTIVE SUMMARY

This report simulates the wireless channels of a low-flying UAV relaying communications between small-unit mobile ground units operating in urban environments. The wireless channels are simulated by the *Numerical Electromagnetics Code-Basic Scattering Code* (NEC-BSC) [16]. This code approximates the 3-D electric field propagating throughout the city to user-specified accuracy. This electric field encompass the digital 3-D city, the multipath propagation, and the antenna patterns of both the UAV and the ground units. Consequently, the simulations represent wireless UAV relay channels with sufficient accuracy to assess *relative* performance shifts.

The UAV platform is modeled after the Coyote equipped with a bottom-mounted whip antenna. The ground-level receivers employ half-wavelength dipoles at 500 MHz. The following following observations summarize this report:

- Antenna patterns of both the UAV and ground units affect the UAV loitering patterns (Section 4).
- City geometry, particularly building height, governs the fading modes: heavy shadowing versus multipath fading (Sections 5 and 6).
- Fluctuating Two-Ray (FTR) fading is a credible model for systems employing 1 MHz or less of bandwidth (Section 7).
- Employing the UAV as a relay simultaneously increases capacity, decreases transmission power but requires the nodes to handle spatially varying channels (Sections 8, 9, 10).

These observations support both the requirements to bring these UAV channels into the network modeling domain of the *Extendable Mobile Ad-hoc Network Emulator* (EMANE) [8]. Long-term payoffs are the understanding how the UAV's broadcasts flow through the city's "spatial filter" [30], [11], [25], [29]. Subsequent reports assess the payoffs delivered by different UAV platforms, more advanced UAV antennas, and multi-antenna systems (MIMO).

This page is intentionally blank.

TABLE OF CONTENTS

Executive Summary iii

1. Overview of the UAV Urban Channel Simulations 1

1.1 Organization of the Report 2

1.2 Varying the Simulations 2

2. Technical Preliminaries 3

2.1 Solving the 3-D Wave Equation 3

2.2 Channel Functions 4

2.3 Fading Models for the UAV Channel 5

2.3.1 Rician Fading 5

2.3.2 Fluctuating Beckmann (FB) Fading 6

2.3.3 Fluctuating Two-Ray (FTR) Fading 6

3. The UAV Platform 7

3.1 The UAV 7

3.2 Bottom-Mounted Whip 8

3.3 UAV Antenna Patterns at 500 MHz 9

4. UAV-to-Street-Level Receivers at 500 MHz 11

4.1 The Digital City 11

4.2 UAV Coverage of the City 12

4.3 Coverage Summary 14

5. UAV Tracks at 500 MHz 15

5.1 Straight-Line Tracks at 100-meter height 15

5.2 Straight-Line Tracks at 150 and 200 meters Height 21

5.3 Fading Summary 22

6. Track Structures in 2-D Vertical Slices at 500 MHz 23

6.1 Vertical Slice at $x_T = 25$ meters 23

6.2 Vertical Slices Moving Downrange 24

6.3 Fading Analysis 28

7. Wideband Tracks at 500 MHz 29

7.1 Widband Tracks at 100-meter Height 29

7.2 Widband Tracks at 200-meter Height 32

7.3 Wideband Channel Summary 33

8. UAV as a Relay 35

8.1 Ground-to-Ground Channels 36

8.2 Ground-to-UAV 37

8.3 Performance Shift Delivered by the UAV Relay 39

9. Circular Tracks 41

9.1 Circular Track at 200 meters 41

9.2 UAV Flying the Circular Track with $0°$ Roll 42
9.3 UAV Flying the Circular Track with $45°$ Roll 43
9.4 Circular Track Summary 44
10. UAV Relay on a Circular Track **45**
10.1 UAV Channels on the Circular Track 45
10.2 Summary of the Relay 48
11. UAV Channels: Summary and Recommendations **49**

List of Figures

1. UAV channel including the antenna pattern of the UAV, the antenna pattern of a street-level receiver, and the city acting as a spatial filter. 1
2. Edge diffraction [17, Figure 2]. 3
3. Coyote employed for hurricane research; launched from the P-3 in the background [18] (Figure courtesy of NOAA). 7
4. UAV model and the local x-y-z coordinate system. 8
5. Wire-frame model of the UAV; The 1-inch bottom-mounted whip is located along the z-axis and directly below the local origin. 8
6. Electric field components in the local coordinates of the UAV. 9
7. E_θ pattern for the 1-inch bottom-mounted whip; zenith angle θ sweeps from straight up $\theta = 0°$ to straight down $\theta = 180°$. 9
8. E_ϕ pattern for the 1-inch bottom-mounted whip; azimuth angle ϕ sweeps from x-axis $\phi = 0°$ toward the y-axis $\phi = 90°$. 10
9. Urban geometry; transmitter is 50 meters above the origin. 11
10. Top view of the 3-D urban model; UAV transmitter is 50 meters above the origin. 12
11. UAV coverage at 500 MHz; UAV transmitter is 50 meters above the origin. 13
12. UAV coverage at 500 MHz; UAV transmitter is 100 meters above the origin. 13
13. UAV coverage at 500 MHz; UAV transmitter is 150 meters above the origin. 14
14. UAV y-axis track at 100 meters height (red line) in the 3-D city; street-level receiver marked by the (blue) "thumbtack" with height exaggerated for clarity 15
15. Top view of the UAV's y-axis track (red line); offset from the y-axis by $x_T = 25$ meters; street-level receiver marked by the (blue) dot. 16
16. Rays from the UAV along the y-axis track to the street-level receiver at x_R=150, y_R=50, z_R=2 meters. The color code shows relative attenuation. 17
17. Delay spread function $h(y_T, \tau)$; UAV flying along the y-axis track broadcasting the street-level receiver at x_R=150, y_R=50, z_R=2 meters. 18
18. Power-delay profile; UAV flying along the y-axis track at 100 meters height broadcasting to the street-level receiver at x_R=150, y_R=50, z_R=2 meters. 18
19. Narrowband channel amplitude from the UAV flying the y-axis track at 100 meters height broadcasting to the street-level receiver. 19
20. Fading models; shadowing in the first part of the track. 20
21. Fading model; multipath in the later part of the track. 20
22. Narrowband channel amplitude from the UAV flying the y-axis at $z_T = 150$ (m) broadcasting to the street-level receiver. 21
23. Narrowband channel amplitude from the UAV flying the y-axis track at $z_T = 200$ (m) broadcasting to the street-level receiver. 21
24. Upper panel: Multipath fading plotted with the slow-fading component. Lower panel: Simulated FTR fading plotted with the slow-fading component. 22
25. UAV channels at 500-MHz to the street-level receiver; UAV is on the slice at $x = +25$ meters. 23
26. UAV channels at 500-MHz; UAV is on the slice at $x_T = +25$ meters. The street-level receiver is at $x_R = 150$, $y_R = 200$, $z_R = 2$ meters. 24
27. 500-MHz channels from the UAV to the street-level receiver; UAV is on the slice at $x_T = -50$ meters. 25
28. UAV channels at 500 MHz in the 3-D city; UAV is on the slice at $x_T = -50$ meters. Street-level receiver is at $x_R = 150$, $y_R = 200$, $z_R = 2$ meters. 25
29. UAV channels at 500 MHz to the street-level receiver; UAV is on the slice at $x_T = -100$ meters. Street-level receiver is at $x_R = 150$, $y_R = 200$, $z_R = 2$ meters. 26

30. UAV channels at 500 MHz in the 3-D city; UAV is on the slice at $x_T = -100$ meters. Street-level receiver is at $x_R = 150$, $y_R = 200$, $z_R = 2$ meters. 26
31. UAV channels at 500 MHz to the street-level receiver; sliced at $x_T = -200$ meters. 27
32. UAV channels at 500 MHz in the 3-D city; UAV in on the slice at $x_T = -200$ meters. Street-level receiver is at $x_R = 150$, $y_R = 200$, $z_R = 2$ meters. 27
33. UAV shadowing geometry. 28
34. The 10-MHz channel centered on 500 MHz; UAV on the track at 100-meter height broadcasting to the street-level receiver. 29
35. Delay spread estimate of the 10-MHz channel centered on 500 MHz; UAV on the track at 100-meter height broadcasting to the street-level receiver; Gaussian window with 1-μs resolution. 31
36. Delay spread estimate of the 10-MHz channel centered on 500 MHz; UAV on the track at 100-meter height broadcasting to the street-level receiver; Gaussian window with 0.5-μs resolution. 31
37. The 10-MHz channel centered on 500 MHz; UAV on the track at 200-meter height broadcasting to the street-level receiver. 32
38. Delay spread estimate of the 10-MHz channel centered on 500 MHz; UAV on the track at 200-meter height broadcasting to the street-level receiver; Gaussian window with 0.5-μs resolution. 33
39. Top view of Node 1 and Node 2. 35
40. Throughput versus power for the ground-to-ground link between Nodes 1 and 2. 36
41. Node-to-UAV channels at 500 MHz. 37
42. The worst Node-to-UAV channel at 500 MHz. 38
43. Histogram of the worst Node-to-UAV channels at 500 MHz; UAV flies at 150 m. 38
44. Relay rate; UAV at $z_T = 150$ (m) height; $f_B = 1$ MHz; $p_\Sigma = 1$ Watt. 39
45. Relay rate; UAV at $z_T = 150$ (m) height; $f_B = 1$ MHz; $p_\Sigma = 0.1$ Watt. 40
46. Circular track and the receiver; the large "thumbtack" marks the location of the street-level receiver. 41
47. Top view of the circular track and the receiver. 42
48. Vertical cross section of the circular track at azimuth $\phi = 180°$ showing the UAV's orientation; $\widehat{\mathbf{x}}$ points out of the paper. 42
49. Channel on the circular track. 43
50. Vertical cross section of the circular track at azimuth $\phi = 180°$ showing the UAV flying with a constant roll of $45°$; $\widehat{\mathbf{x}}$ points out of the paper. 43
51. Channel on the circular track; UAV rolled $45°$. 44
52. Top view of the circular track and the two nodes. 45
53. Channel on the circular track at Node 1. 46
54. Channel on the circular track at Node 2. 46
55. Worst channel relay on the circular track. 47
56. Histogram of the worst channel throughput on the circular track; equal-power allocation; $p_\Sigma = 1$ Watt. 48

List of Tables

1. Second-order diffraction terms. 4
2. Diffraction terms for the urban simulation. 4
3. Coyote performance and specifications. 7
4. Dielectrics for the 3-D urban simulation at 500 MHz. 12

This page is intentionally left blank

1. OVERVIEW OF THE UAV URBAN CHANNEL SIMULATIONS

This report simulates ground-to-air wireless channels of a low-flying UAV supporting small-unit mobile ground forces deployed in urban environments. Figure 1 is a block diagram of these simulations showing the city acting as a spatial filter between the UAV and a street-level receiver. The UAV channels are measured from the *input terminals* feeding the antenna on the UAV to the *output terminals* at the street-level receivers. These channels encompass the UAV's antenna with platform effects, the multipath propagation though the city, and the electric field surrounding the receiver's antenna.

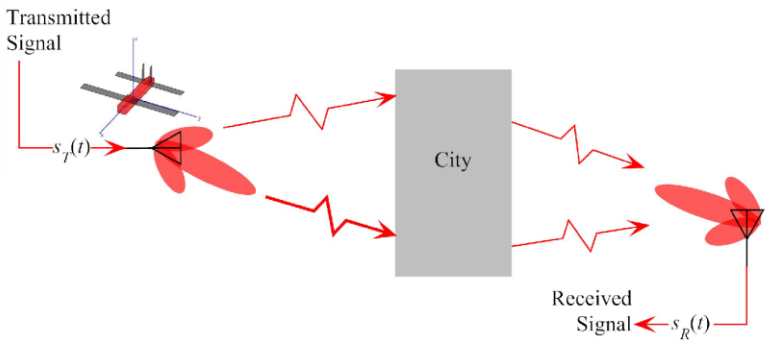

Figure 1. UAV channel including the antenna pattern of the UAV, the antenna pattern of a street-level receiver, and the city acting as a spatial filter.

Figure 1 shows the UAV channel consists of multiple rays carrying the transmitted signal $s_T(t)$ from the UAV location $\mathbf{r}_T$ to the received signal $s_R(t)$ at the street-level location $\mathbf{r}_R$. A multipath model of this channel is

$$s_R(t) = \sum_{\ell=1}^{L} h_\ell(f_C; \mathbf{r}_T, \mathbf{r}_R) \cdot s_T(t - \tau_\ell), \tag{1}$$

where the ℓ-th ray *delays* the signal by τ_ℓ and *fades* the signal by $h_\ell(f_C; \mathbf{r}_T, \mathbf{r}_R)$. The multiplication by the fading implies a narrow-band signal at center frequency f_C. As the UAV flies through the 3-D space, the time-varying position of the UAV at location $\mathbf{r}_T(t)$ generates time-varying UAV channels of the form

$$s_R(t) = \sum_{\ell=1}^{L} h_\ell(f_C; \mathbf{r}_T(t), \mathbf{r}_R) s_T(\tau - \tau_\ell(t)). \tag{2}$$

These time-varying UAV channels are the "objects of discussion" of this report. When these UAV channels form a relay between street-level receivers, these channels average 30 dB less loss than ground-to-ground channels connecting the same receivers. Assuming urban noise, these UAV relays increase throughput by a factor of 8 over ground-level channels. These simulated gains are limited by the following assumptions:

- Fidelity of the 3-D city
- Throughput is computed from the capacity equation,
- Latency is not simulated,
- Urban interference is not modeled.

Despite these limitations, the simulated 30 dB performance shift argues that actual UAV relays will deliver significant performance shifts over ground-to-ground links.

1.1 ORGANIZATION OF THE REPORT

Section 2 reviews necessary technical background: the 3-D wave equation solver, channel functions, and fading models relevant to the time-varying wireless channels.

Section 3 details the UAV, the bottom-mounted whip antenna, and the resulting antenna patterns. These patterns determine the complex-valued electric field around the UAV that broadcasts into the city and produces multiple rays arriving at the street-level receivers. Each ray interacts with the receiver's antenna to generate a complex-valued voltage at the antenna's output terminals. The *coherent* sum of these voltages determines the channel of Equation 1.

Section 4 shows the UAV "illuminating" the city from a hovering position. The resulting coverage plots show that the fading caused by the city's geometry fall into two distinct regions: (*i*) heavily shadowed regions, (*ii*) multipath regions. Varying the UAV height and location reduces blockage while the multipath requires the radio systems adapt to the channel.

Section 5 "flies" the UAV along horizontal straight-line tracks while broadcasting to a fixed, street-level receiver. The UAV channels along these tracks exhibit rapid "switching" between regions of heavy shadowing and multipath fading. Gamma fading is identified as a fading model for the heavily shadowed regions. Generalized Rician fading is a credible as a fading model in the multipath regions. Physical explanations for these fading models are given in the next two sections.

Section 6 explains the fading regions. By stacking hundreds of these horizontal tracks, a vertical "slice" of the channel is produced. These slices reveal how the city's geometry causes non-stationary channel features. In particular, blockage by buildings produces regions of heavy shadowing. Raising the UAV height reduces the shadowing regions. The resulting unblocked fading is well-modeled by the classic two-ray interference as verified by an analysis of the wideband UAV channel.

Section 7 examines *wideband* UAV channels along the UAV tracks. Estimates of the channel's *delay spread function* shows the Two-Ray Fluctuating Rician fading is a credible fading model.

The final sections compare the UAV relay against the ground-to-ground links. Section 8 uses the coverage plots to assess the payoff when the UAV is employed as a relay. The scenario assumes the UAV is loitering over two street-level transceivers. Even the simplest of power allocations shows that the UAV relay boosts throughput over the ground-to-ground link. Section 9 lays out a circular track and the associated channels to a single ground node. Section 10 employs this circular track to relay between the two street-level transceivers of Section 8. The UAV's relay performance on this circular track also shows significant improvement over the ground-to-ground link. Section 11 closes with highlights of the UAV channels:

- pattern and coverage,
- tactical operational height and city geometry,
- generalized Rician fading,
- UAV relay performance.

These highlights guide simulations to reveal the performance shifts available from UAV channels especially with respect to stealthy wireless networks.

1.2 VARYING THE SIMULATIONS

This report presents a framework to assess performance shifts in the ground-to-air channels of a low-flying UAV relay operating over an urban environment. Swapping out system components in this framework provides an "apples-to-apples" assessment of the relative performance shift. The antennas may be swapped out for assessments of antenna placement, antenna designs, antenna polarizations, and multiple antennas. The UAV flight patterns may be altered for assessments of UAV deployment (e.g., altitude versus coverage; loitering patterns for multiple UAVs). The city model may be swapped out to assess how the city geometry (e.g., building height, street width) affects the shadowing and blockage.

2. TECHNICAL PRELIMINARIES

This report models ground-to-air channels of a low-flying UAV operating over a an urban environment. The first task of channel modeling is to simulate the UAV's transmissions propagating through the urban environment. This propagation is governed by 3-D wave equation. Section 2.1 reviews a 3-D wave equation solver suitable for kilometer-sized regions. This solver approximates the UAV channels given by Equation 1. The second task of channel modeling extracts the fading of the time-varying channels as the UAV flies over the city from Equation 2. Section 2.2 reviews the formalism of the time-varying channels. This simulated fading is well-modeled as multi-ray Rician subject to shadowing. Section 2.3 reviews Rician fading and generalizations.

2.1 SOLVING THE 3-D WAVE EQUATION

Figure 1 makes explicit that the UAV channels start at the input to the UAV antenna, propagate through the 3-D city, and finish at the output the receive antenna. The propagation through the 3-D city is governed by the wave equation [9, Chapter 3]. The *Numerical Electromagnetics Code-Basic Scattering Code* (NEC-BSC) computes approximate solutions to the 3-D wave equation in complex environments by reflection and diffraction modeling [16]. The electric field at position $\mathbf{r}$ generated by a transmitter broadcasting at frequency f is the sum of multiple rays interacting with the 3-D environment:

$$\begin{aligned}\mathbf{E}(f;\mathbf{r}) &= \mathbf{E}_{\text{inc}}(f) + \sum_{r\in\mathcal{P}(\mathbf{r})} \mathbf{E}^{p}(f;\mathbf{q}_r) + \sum_{e\in\mathcal{E}(\mathbf{r})} \mathbf{E}^{e}(f;\mathbf{q}_e) \\ &+ \sum_{v\in\mathcal{V}(\mathbf{r})} \mathbf{E}^{v}(f;\mathbf{q}_v) + \text{higher-order terms.} \end{aligned} \tag{3}$$

The first term is the incident electric field $\mathbf{E}_{\text{inc}}$ produced by the direct path from the source to position $\mathbf{r}$, provided there is no blockage. The second term sums each electric field generated by the ray traveling from the source, reflecting off a plate at position $\mathbf{q}_r$, and arriving at position $\mathbf{r}$. Each plate reflection models the dielectric of the plate and consequent spreading factor after reflection. The third term sums each electric field generated by the ray traveling from the source, diffracting on an edge at position $\mathbf{q}_e$, and arriving at position $\mathbf{r}$. The edge diffraction terms correct for discontinuities in the incident and plate-reflected fields. Figure 2 illustrates the diffraction-cone geometry for an edge. Each edge diffraction models the dielectric of the edge and consequent spreading factor after diffraction. The fourth term sums each electric field caused by rays traveling from the source, diffracting at vertex $\mathbf{q}_v$, and arriving position $\mathbf{r}$. The vertex diffraction terms correct for the discontinuities in the edge-diffracted fields.

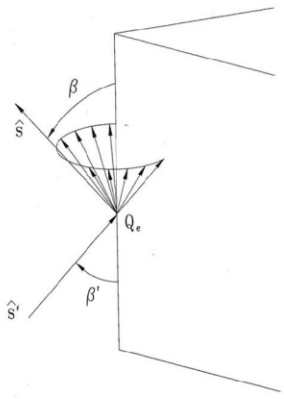

Figure 2. Edge diffraction [17, Figure 2].

Multiple interactions between flat faces, edges, and vertices are needed for complex environments. Cascading these interactions determine the higher-order interactions. The higher-order terms compensate discontinuities in first-order and other lower-order terms. Table 1 lists the second-order interactions.

Table 1. Second-order diffraction terms.

Plate-to-plate	Edge-to-plate	Vertex-to-plate
Plate-to-edge	Edge-to-edge	Vertex-to-edge
Plate-to-vertex	Edge-to-vertex	Vertex-to-vertex

Third-order terms follow a similar pattern (e.g., Plate-to-plate-to-plate, Plate-to-plate-to-edge, ...). Complex environments have an infinite number of higher-order interactions. A correct application of NEC-BSC requires that the dominant terms in an environment be determined to guarantee accuracy of the solution. Such a convergence study was undertaken to support the propagation in [7]. Table 2 lists the diffraction terms necessary to approximate the electric field to 30-dB accuracy. The dominant terms were limited to plate and edge interactions.

Table 2. Diffraction terms for the urban simulation.

Order	Terms
0	Incident
1	Plate, edge
2	Plate-to-plate, Edge-to-plate, Edge-to-edge

2.2 CHANNEL FUNCTIONS

A classic model of the time-varying channel is the *delay spread* function $\{h(t,\tau)\}$ mapping a transmitted signal $s_T(t)$ to a received signal $s_R(t)$ as [5]:

$$s_R(t) = \int_{-\infty}^{\infty} h(t,\tau) s_T(t-\tau) d\tau. \tag{4}$$

A classic model of a delay spread function is adapted from [21, Eq. 14-1-5]:

$$h(t,\tau) = \sum_{\ell=1}^{L} h_\ell(t)\delta(\tau - \tau_\ell). \tag{5}$$

Inserting the delay spread function of Equation 5 into Equation 4 models the received signal $s_R(t)$ as the sum of delayed and faded copies of the transmitted signal $s_T(t)$:

$$s_R(t) = \sum_{\ell=1}^{L} h_\ell(t) s_T(t-\tau_\ell).$$

If the fading processes $\{h_\ell(t)\}$ are wide-sense stationary, uncorrelated, and ergodic [19]:

$$E[|h_\ell(t)|^2] = \lim_{T\to\infty} \frac{1}{T} \int_{-T}^{T} |h_\ell(t)|^2 dt \quad \text{(a.s.)}$$

and the delays τ_l are deterministic, the average power over time in the delay spread function of Equation 5 is the *power-delay profile* [27, page 77]:

$$P_h(\tau) = E[|h(t,\tau)|^2] = \sum_{\ell=1}^{L} E[|h_\ell(t)|^2]\ \delta(\tau - \tau_\ell).$$

This power-delay profile shows the fading power at each delay.

If the UAV is moving as in Equation 2, the delay spread function has the form [21, Eq. 14-1-5]:

$$h(t,\tau) = \sum_{\ell=1}^{L} h_\ell(t)\delta(\tau - \tau_\ell(t)). \tag{6}$$

Equation 3 computes each term in this fading model as a function of the UAV's time-varying location $\mathbf{r}_T(t)$: each multpath ray has delay $\tau_\ell(t)$ computable from the ray's length; each fading process $h_\ell(t)$ is computable from the electric field. Averaging the power of the delay spread function of Equation 6 over time produces the *power-delay profile* of the form

$$P_h(\tau) = E[|h(t,\tau)|^2] = \sum_{\ell=1}^{L} E[|h_\ell(t)|^2]\, p_\ell(\tau),$$

where $p_\ell(\tau)$ is the probability density of the random delay τ_ℓ, provided the fading processes $\{h_\ell(t)\}$ are uncorrelated, ergodic, and independent of the delay processes $\{\tau_\ell(t)\}$ are uncorrelated and ergodic. This power-delay profile shows the fading power spread over the distribution of each delay.

2.3 FADING MODELS FOR THE UAV CHANNEL

The simulated UAV channels exhibit generalized Rician fading on the ray paths, in addition to the heavy shadowing caused by urban blockage. Section 2.3.1 reviews Rician fading. Section 2.3.2 introduces multi-ray Rician fading where each specular component is modulated by a fluctuating process to produce Fluctuating Beckman fading. Section 2.3.3 specializes Fluctuating Beckman fading to two rays. The payoff is that this Fluctuating Two-Ray fading is a credible model of the multipath fading observed on the UAV tracks in Section 5.

2.3.1 Rician Fading

Rician fading is succinctly described by Stüber as the complex-valued Gaussian process [27, page 51]

$$h(t) = s_{\mathsf{LOS}} + g(t),$$

where s_{LOS} is the complex-valued *specular component* and the $\{g(t)\}$ is the *diffuse component* is complex-valued Gaussian process

$$g(t) = g_I(t) + jg_Q(t)$$

consisting of the sum of two real-valued, zero-mean, independent, stationary Gaussian processes $\{g_I(t)\}$ and $\{g_Q(t)\}$ with common variance σ^2. The average power in the fading is the sum of the specular and diffuse powers [27, page 53]

$$\Omega = E[|h(t)|^2] = |s_{\mathsf{LOS}}|^2 + 2\sigma^2$$

The Rician K factor is ratio of the specular to the scattered power [27, page 53]

$$K = 10 \cdot \log_{10}\left(\frac{|s_{\mathsf{LOS}}|^2}{2\sigma^2}\right) \quad \text{[dB]}.$$

The probability distribution of $\{|h(t)|\}$ is [21, Eq. 2-1-141], [27, Eq. 2.45]

$$p_{|h|}(r) = \frac{r}{\sigma^2}\exp\left(-\frac{r^2+s^2}{2\sigma^2}\right) I_0\left(\frac{rs}{\sigma^2}\right),$$

where $I_0(r)$ denotes the modified Bessel function of the first kind.

2.3.2 Fluctuating Beckmann (FB) Fading

There exists a multitude of Rician fading generalizations. Proakis generalizes the Rician fading by increasing the number of Rician processes [21]. The Fluctuating Beckmann (FB) fading generalizes multi-path Rician fading by fluctuating the power of each specular component of the Rician processes. The fading is adapted from [22, Eq. 1]:

$$h_{\mathsf{FB}}(t) = \sum_{\ell=1}^{L} \xi(t) s_\ell + g_\ell(t).$$

Specular Power: Each specular component s_ℓ is subject to a fluctuation by the Nakagami-m distributed random process $\{\xi(t)\}$ with shape parameter m and $E[\xi(t)^2] = 1$. This model forces all the specular components to be subject to the same fluctuations.

Scattered Power: Each diffuse component $\{g_\ell(t)\}$ is modeled as

$$g_\ell(t) = X_\ell(t) + jY_\ell(t)$$

where $\{X_\ell(t)\}$ and $\{Y_\ell(t)\}$ are real-valued, mutually independent, stationary Gaussian random processes with zero mean and imbalanced variances:

$$E[|X_\ell(t)|^2] = \sigma_X^2, \quad E[|Y_\ell(t)|^2] = \sigma_Y^2.$$

This FB fading forces the all the diffuse components to be modeled by the same Gaussian process.

K Factor: The Rician K factor is generalized to be the ratio of the specular to the scattered powers [22, Eq. 2]:

$$\kappa = \frac{\sum_{\ell=1}^{L} |s_\ell|^2}{L \times (\sigma_X^2 + \sigma_Y^2)}.$$

2.3.3 Fluctuating Two-Ray (FTR) Fading

A simpler fading model that aligns well with the simulated UAV channels in this report is is Fluctuating Two-Ray (FTR) Fading that employs only two fluctuating Rician rays [23, Eq. 2]:

$$h_{\mathsf{FTR}}(t) = \sqrt{\zeta(t)}\{s_1 + s_2\} \; + \; g(t)$$

Specular Power: As in FB fading, the fluctuations apply to both specular components s_1 and s_2. The fluctuations are modeled as a Nakagami-m random processes $\{\zeta(t)\}$ with a squared unit-mean $E[|\zeta(t)|^2] = 1$ or, equivalently, a Gamma distributed random variable with probability distribution [23, Eq. 3]

$$p_\zeta(u) := \frac{m^m u^{m-1}}{\Gamma(m)} e^{-mu}.$$

Scattered Power: The complex-valued, zero-mean, stationary Gaussian process $X(t) + jY(t)$ models the "combined reception of numerous weak, independently-phased scattered waves" with

$$E[|X(t)|^2], E[|Y(t)|^2] = \sigma^2.$$

Although FTR fading is a special case of FB fading, the former paper offers the following insight with respect to shadowing and this report that calls out as "heavy shadowing" [23]:

> the word "shadowing" was used when the models [1, 20] were introduced, these models should not necessarily be linked to the large-scale fading phenomena also called shadowing, due to a complete or partial blockage by obstacles many times larger than the signal wavelength. Instead, these models reflect any amplitude fluctuation in the specular waves (e.g., say human-body shadowing, variations in the propagation condition, or fast moving scatterers) that takes place over the time period of interest.

3. THE UAV PLATFORM

This section selects a UAV platform, an antenna, an antenna location on the platform, and computes the resulting antenna patterns. The antenna patterns are placed in the 3-D digital city and carry the UAV's broadcasts to the street-level receivers as computed by NEC-BSC. Section 3.1 selects the *Coyote* as the UAV platform. Section 3.2 selects a bottom-mounted 1-inch whip antenna. Section 3.3 shows the vertical and horizontal antenna patterns shaped by the UAV's geometry. Features of these patterns verify that the UAV is correctly placed and oriented in the 3-D simulations.

3.1 THE UAV

The Coyote was developed by BAE under an ONR grant for Intelligence, Surveillance, and Reconnaissance (ISR) operations. The typical ISR payloads are Electro-Optical (EO) or Infra-Red (IR) cameras and data transmitters. Figure 3 shows a Coyote used for weather research and the P-3 aircraft that serves as the launch platform. Table 3 details the standard Coyote performance bounds.

Figure 3. Coyote employed for hurricane research; launched from the P-3 in the background [18] (Figure courtesy of NOAA).

Table 3. Coyote performance and specifications.

Specifications	Performance
Endurance	90 minutes ISR collection
Max Altitude	20,000 ft AGL
Speed	60–85 knots
Weight	12–14 pounds
Wing Span	58 inches
Length	3 feet (approximately)
Control	line-of-sight radio link (VHF or UHF)

3.2 BOTTOM-MOUNTED WHIP

Figure 4 shows the Coyote modeled in NEC-BSC with its local coordinate system that orients the vehicle in the NEC-BSC simulations.

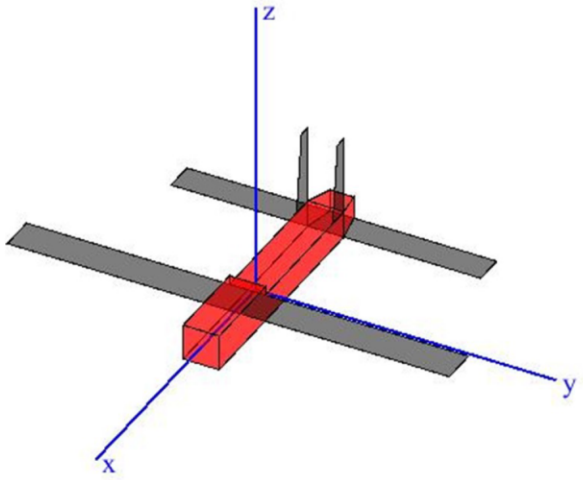

Figure 4. UAV model and the local x-y-z coordinate system.

Figure 5 shows the wire-frame model of the UAV and the whip antenna mounted on the underside of the UAV. The next section shows the UAV platform modifies the free-space pattern of the whip antenna.

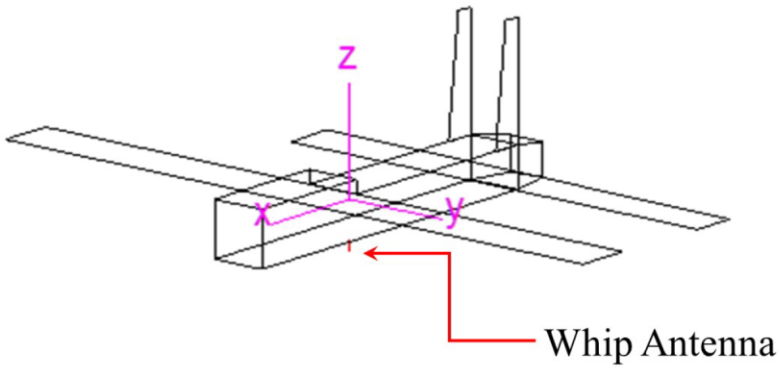

Figure 5. Wire-frame model of the UAV; The 1-inch bottom-mounted whip is located along the z-axis and directly below the local origin.

3.3 UAV ANTENNA PATTERNS AT 500 MHZ

Figure 6 is the coordinate system on the UAV that defines the electric field of the antenna. Figures 7 and 8 show the vertical E_θ and horizontal E_ϕ electric fields of the antenna. The whip exhibits relatively strong vertical polarization radiating in the downward hemisphere and broadcasting from the nose and tail. The horizontal discontinuity in both patterns at zenith $\theta = 90°$ is caused by mounting the antenna on the underside of the UAV. There is a discontinuity in the vertical pattern out the nose ($\phi = 0°, 360°$) for $0° \leq \theta \leq 180°$. The next section uses the discontinuities in these antenna patterns to verify correct alignment of the UAV in the NEC-BSC simulations.

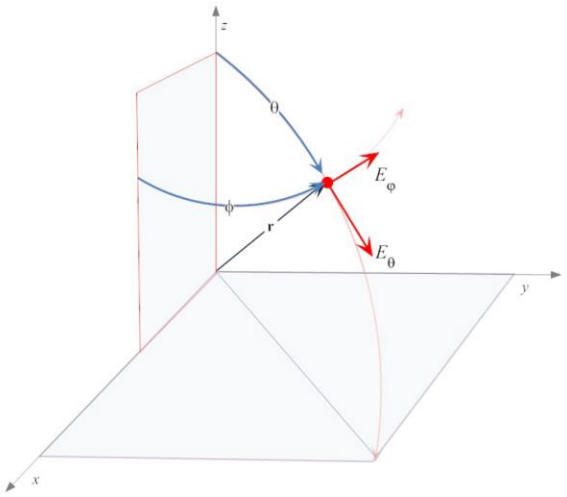

Figure 6. Electric field components in the local coordinates of the UAV.

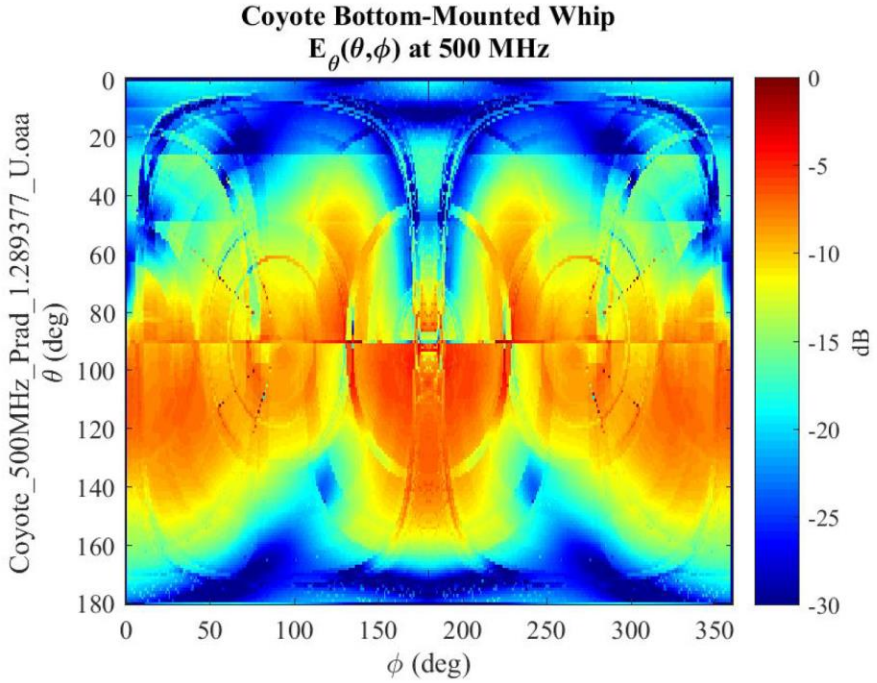

Figure 7. E_θ pattern for the 1-inch bottom-mounted whip; zenith angle θ sweeps from straight up $\theta = 0°$ to straight down $\theta = 180°$.

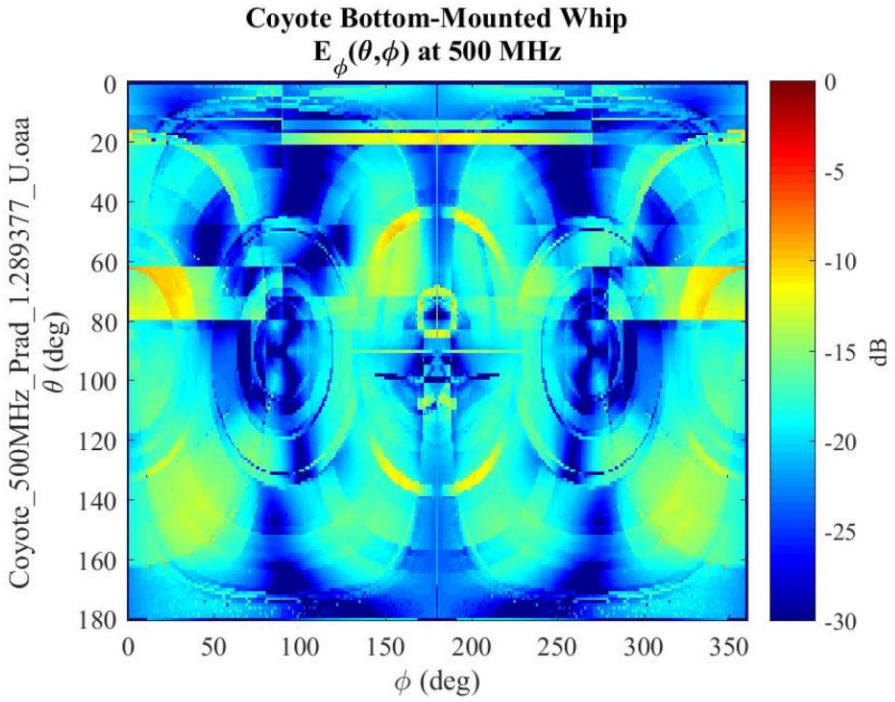

Figure 8. E_ϕ pattern for the 1-inch bottom-mounted whip; azimuth angle ϕ sweeps from x-axis $\phi = 0°$ toward the y-axis $\phi = 90°$.

4. UAV-TO-STREET-LEVEL RECEIVERS AT 500 MHZ

This section describes the "coverage" that a UAV hovering over a fixed location delivers to street-level receivers operating within a few city blocks. Section 4.1 introduces the 3-D digital city where the UAV transmitter hovers over the origin. Section 4.2 compares the channels from the UAV to street-level receivers. By varying the height of the UAV, the coverage plots show the varying power levels, shadowing effects of the buildings, and the antenna pattern of the UAV. These simulations verify the UAV's antenna pattern is correctly integrated into the NEC-BSC simulations.

4.1 THE DIGITAL CITY

Figures 9 and 10 show the geometry of the digital city in a 3-D view and a top-down view, respectively. The UAV is located directly over the origin and broadcasts to street-level receivers.

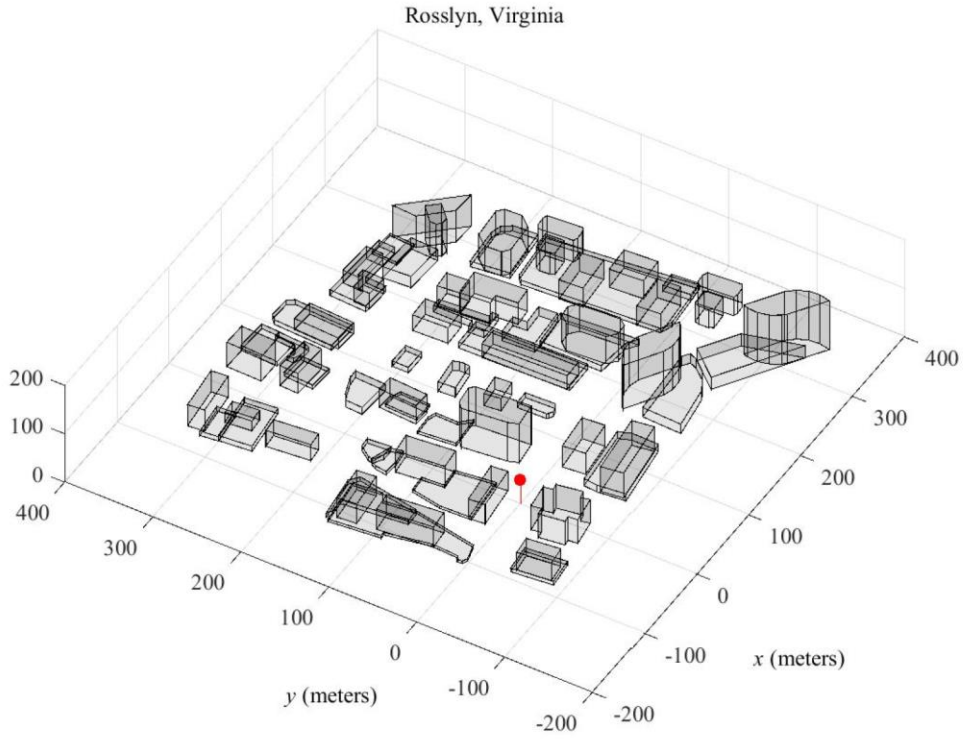

Figure 9. Urban geometry; transmitter is 50 meters above the origin.

The RF propagation in this 3-D city is modeled by NEC-BSC. The propagation code coherently sums multiple reflections and diffractions produced by the UAV's transmissions to *approximate* the 3-D wave equation. The reflections and diffractions are governed by the dielectrics of the building and the ground listed in Table 4. The buildings are modeled with roofs and sides as concrete slabs 0.3 meters thick. Windows, iron reinforcements, building features, foliage, and street structures are not modeled. The ground plane is modeled as a half-plane of asphalt. Consequently, this 3-D urban model produces *representative* RF environments. These RF environments model large-scale multi-path behaviors rather than absolute levels [7]. As such, the channels produced by these simulations are best employed to reveal *relative* performance shifts produced by changing of UAV altitude, orientation, frequency, and bandwidth.

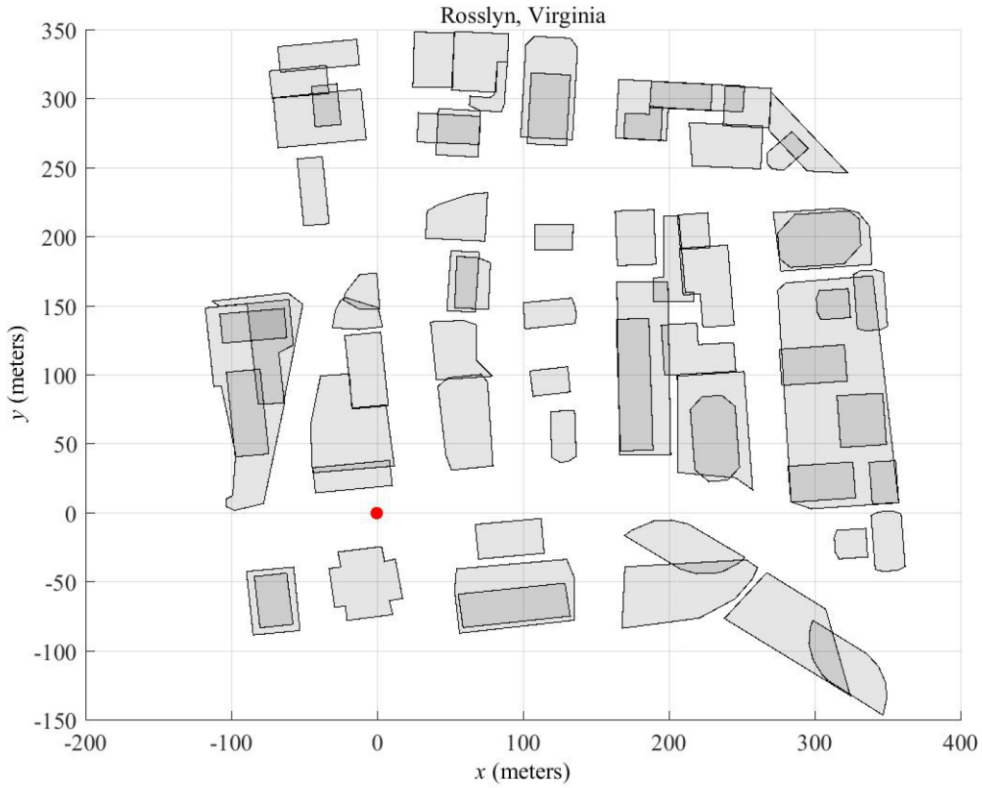

Figure 10. Top view of the 3-D urban model; UAV transmitter is 50 meters above the origin.

Table 4. Dielectrics for the 3-D urban simulation at 500 MHz.

	Slab thickness	Relative Permittivity	Conductivity	Loss Tangent	References
Buildings	0.3 (m)	6.0	0.01 (S/m)	—	[6]
Asphalt	Half plane	2.56	—	0.0011	[24, 4-30]

4.2 UAV COVERAGE OF THE CITY

Figures 11, 12, and 13 plot the channel magnitude $|h(f_C; \mathbf{r}_T, \mathbf{r}_R)|^2$ of Equation 1 as a function of the position $\mathbf{r}_T$ of the UAV and the position $\mathbf{r}_R$ of the receiver at $f_C = 500$ MHz:

$$\begin{cases} \mathbf{r}_T = \begin{bmatrix} 0 & 0 & z_T \end{bmatrix}^{\mathsf{T}} & z_T = 50, 100, 150 \ \text{[m]} \\ \mathbf{r}_R = \begin{bmatrix} x_R & y_R & z_R \end{bmatrix}^{\mathsf{T}} & z_R = 2 \ \text{[m]} \end{cases}.$$

The channel takes the signal from the input terminals to the bottom-mounted 1-inch whip to the output terminals of the street level receiver's half-wavelength (0.3 m) vertical dipoles operating two meters above the street. The UAV is aligned with the city's coordinate system: the nose of the UAV is parallel to the city's x axis, the wings of the UAV align with the city's y axis, and the UAV is level. Figure 7 shows the UAV antenna pattern is almost vertically polarized with a characteristic "gap" in the local x direction. This gap is observed in all the coverage plots where a line is seen running from the origin parallel to the city's x axis. This gap is caused by the discontinuity in the vertical antenna pattern out the nose of the UAV (See Section 3.3). Likewise, all coverage plots show the null produced by the bottom-mounted antenna located over the origin. These observations provide some verification that the UAV's antenna pattern is correctly integrated into NEC-BSC.

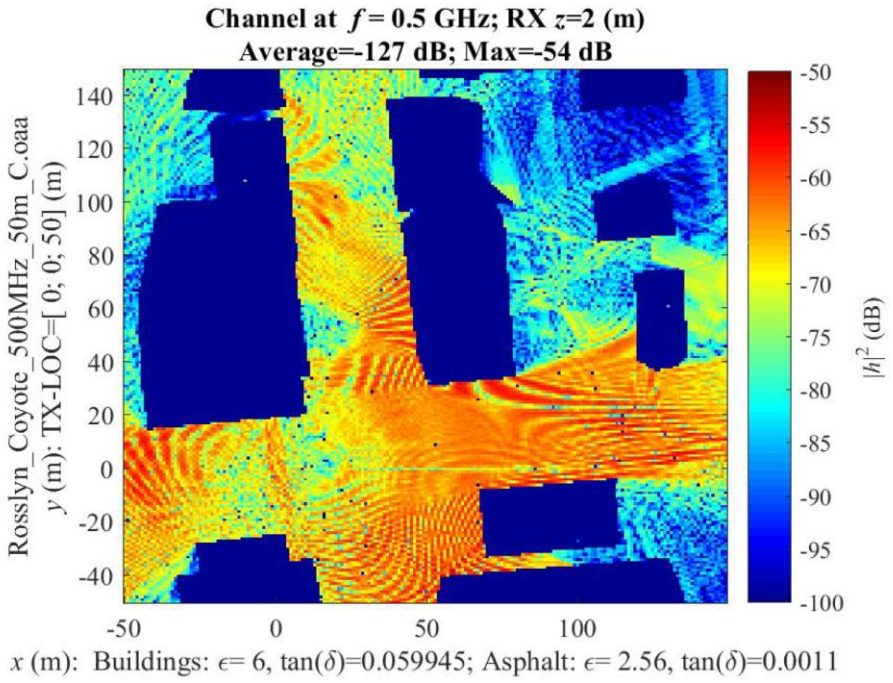

Figure 11. UAV coverage at 500 MHz; UAV transmitter is 50 meters above the origin.

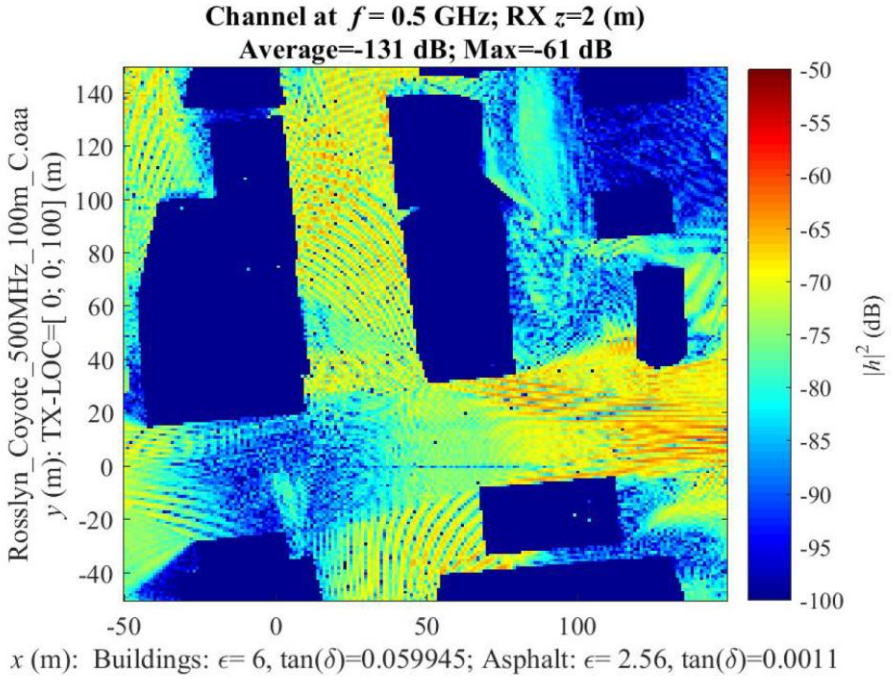

Figure 12. UAV coverage at 500 MHz; UAV transmitter is 100 meters above the origin.

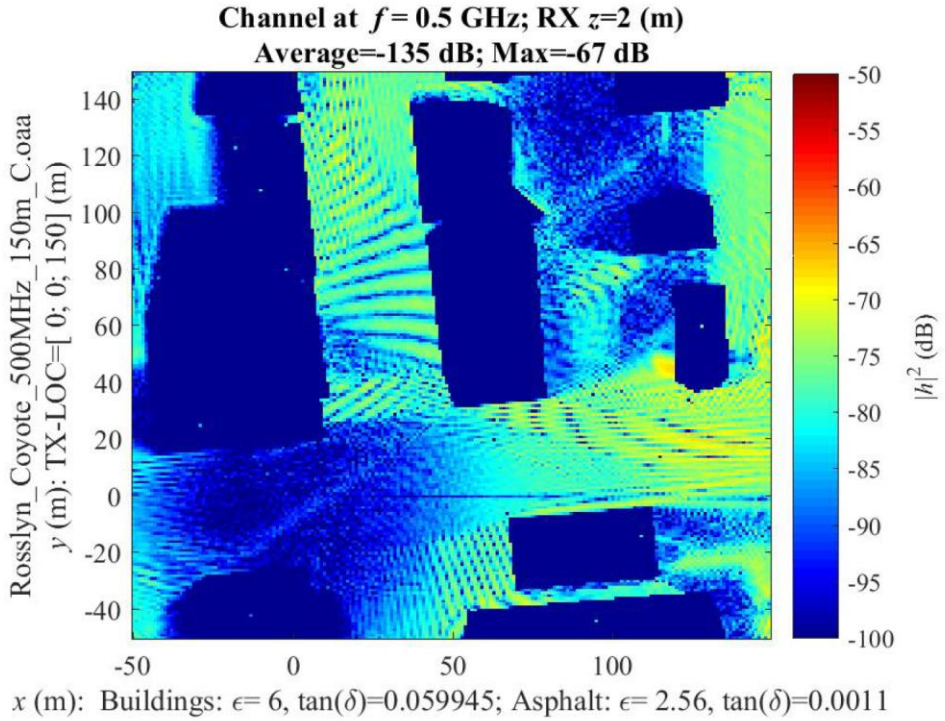

Figure 13. UAV coverage at 500 MHz; UAV transmitter is 150 meters above the origin.

4.3 COVERAGE SUMMARY

The first observation about the coverage plots is that features of the UAV's antenna patterns support the claim that the UAV or, equivalently, the antenna patterns are correctly placed in the simulations. Assuming correct placement, the second observation is that these coverage plots reveal multiple trade-offs that arise as a function of the UAV height.

G-1 The null in the bottom-mounted antenna expands with increasing height.

G-2 Increasing height does not increase coverage until the UAV height exceeds the average building height.

G-3 Increasing height decreases the average channel strength.

These coverage plots assume the UAV is *stationary* over the origin and illuminating the street-level receivers in the city. The next simulations employ a *moving* UAV and *stationary* receivers.

5. UAV TRACKS AT 500 MHZ

This section presents air-to-ground channels as the UAV flies along tracks parallel to the y-axis while broadcasting to a fixed street-level receiver. The channels show a dense multipath and distinct propagation regimes that vary with height. Section 5.1 identifies Rician fading as a credible model for the multipath when there is minimal blockage, When there is heavy shadowing or blockage—distinct from log-normal shadowing—Gamma fading is identified as a model for this propagation regime. Section 5.2 shows that increasing the height of the UAV's tracks cause the fading regimes to change. Section 5.3 compares the fading of all the tracks and identifies Fluctuating Two-Ray fading as a credible fading model for the multipath regimes.

5.1 STRAIGHT-LINE TRACKS AT 100-METER HEIGHT

Figure 14 shows the UAV track parallel to the y-axis at 100-meters height and locates the UAV on the track as follows:

$$\mathbf{r}_T = \begin{bmatrix} x_T \\ y_T \\ z_T \end{bmatrix} = \begin{bmatrix} 25 \\ y_T \\ 100 \end{bmatrix}; \quad 0 \le y_T \le 300 \text{ [m]}.$$

Referring to the UAV's coordinate system in Figure 5, the UAV flies along this track with its nose aligned with the y axis, its wings aligned with the x axis, and the bottom-mounted antenna pointing straight down.

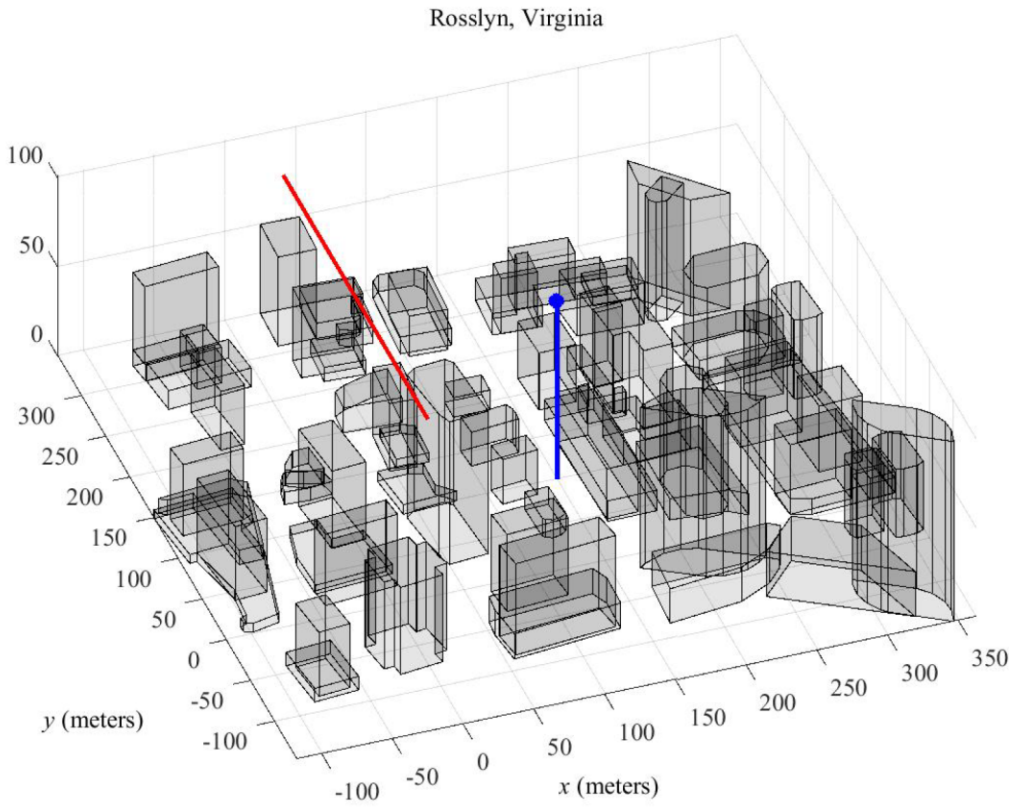

Figure 14. UAV y-axis track at 100 meters height (red line) in the 3-D city; street-level receiver marked by the (blue) "thumbtack" with height exaggerated for clarity

Figure 15 presents the top view of the UAV track and shows the x-axis offset to avoid buildings. The UAV broadcasts to a street-level receiver at the fixed location:

$$\mathbf{r}_R^{\mathsf{T}} = \begin{bmatrix} 150 & 200 & 2 \end{bmatrix}.$$

This receiver is equipped with a half-wavelength (0.3 m) vertical dipole operating 2 meters above the street.

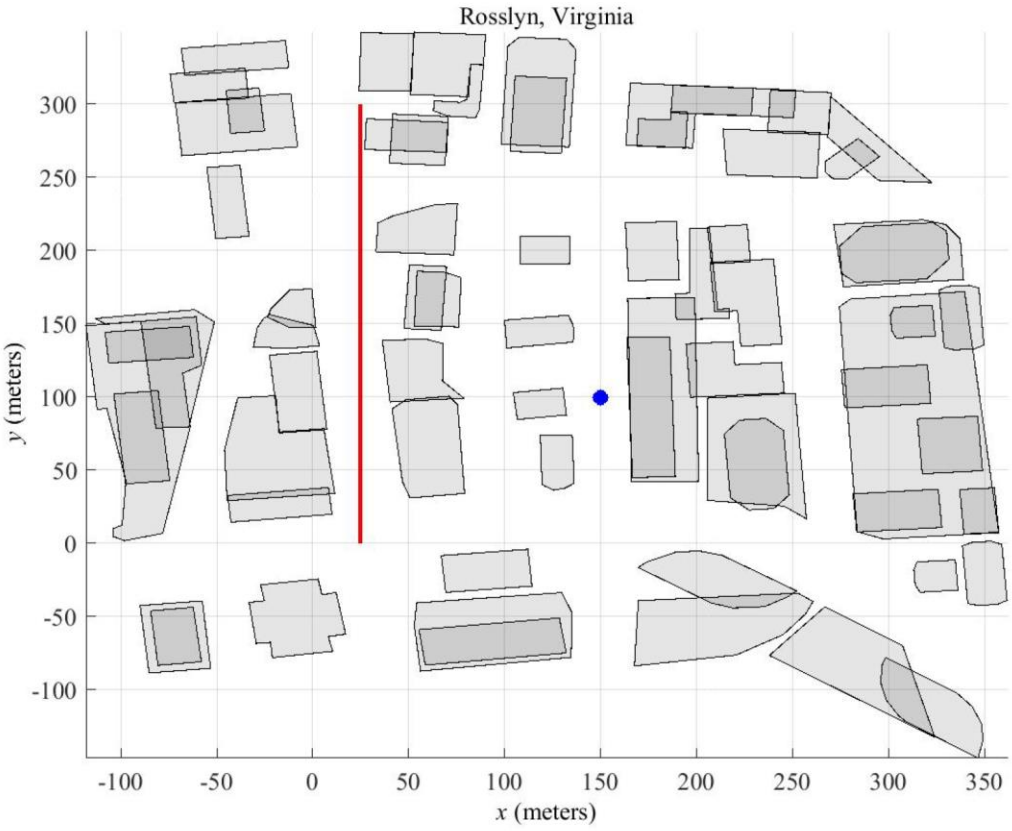

Figure 15. Top view of the UAV's y-axis track (red line); offset from the y-axis by $x_T = 25$ meters; street-level receiver marked by the (blue) dot.

Figure 16 plots the rays at selected points along the track. The figure shows that the channel gets stronger as the UAV travels along the track because there is less blockage and shadowing by the buildings.

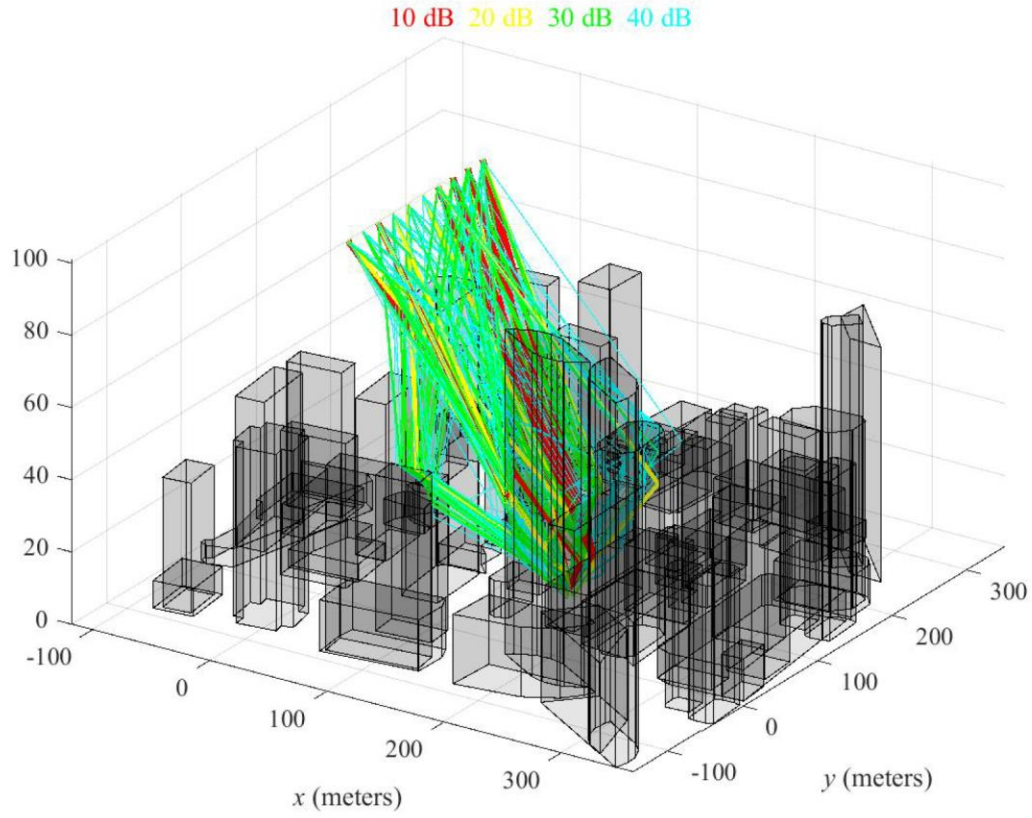

Figure 16. Rays from the UAV along the y-axis track to the street-level receiver at x_R=150, y_R=50, z_R=2 meters. The color code shows relative attenuation.

Figure 17 shows the resulting channel ensemble as a function of the UAV's position along the y-axis track:

$$h(y_T;\tau) = \sum_{\ell=1}^{L} h_\ell(y_T)\delta(\tau - \tau_\ell(y_T)) \tag{7}$$

and is analogous to the delay spread function of Equation 6 except y_T is the variable that indexes each channel rather than time t. This image shows the channel consists of a few strong paths spread between 0.5 and 1.5 μ-sec. Figure 18 is an estimate of *power-delay profile* computed by averaging the delay spread function along the y axis. The power-delay profile verifies that this UAV channel is spread in delay from 0.5 to 1.5 μ-sec and consists of two strong paths. Further discussion requires a bandwidth assumption.

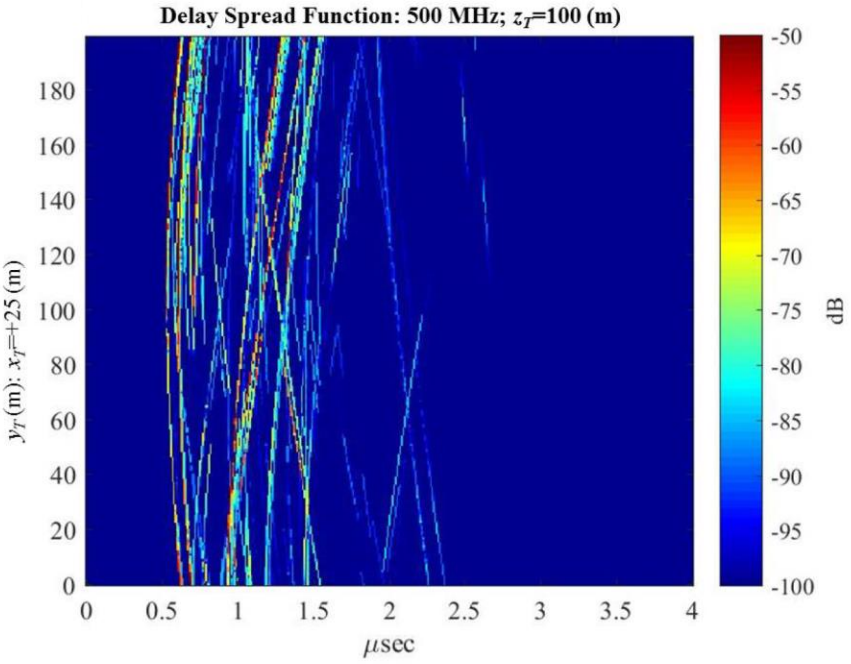

Figure 17. Delay spread function $h(y_T, \tau)$; UAV flying along the y-axis track broadcasting the street-level receiver at x_R=150, y_R=50, z_R=2 meters.

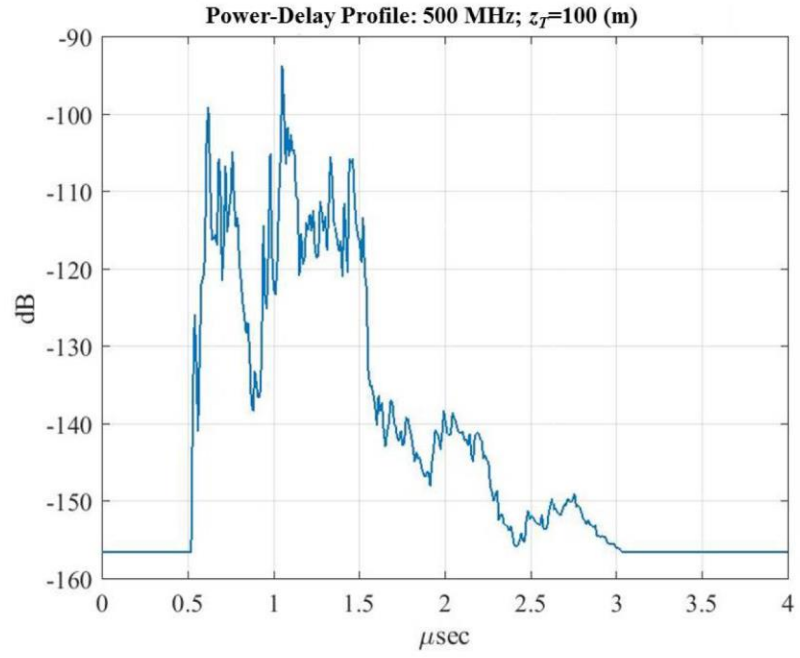

Figure 18. Power-delay profile; UAV flying along the y-axis track at 100 meters height broadcasting to the street-level receiver at x_R=150, y_R=50, z_R=2 meters.

If the channel is modeled assuming a bandwidth f_B of 1 MHz or less, the strong paths in the delay region from 0.5 to 1.5 μs cannot be resolved. Therefore, one narrowband channel approximation of Equation 7 is

$$h_{\mathrm{NB}}(y_T;\tau) = \left\{ \sum_{\ell=1}^{L} h_\ell(y_T) \right\} \delta(\tau - \tau_0),$$

where the gross delay is $\tau_0 = 1$ μs. Figure 19 plots the magnitude of this channel as a function of the UAV's position along the 50-meter track. There are two distinct fading regimes

- Heavy shadowing: $0 \leq y_T \leq 140$ meters,
- Multipath fading: $140 \leq y_T \leq 300$ meters.

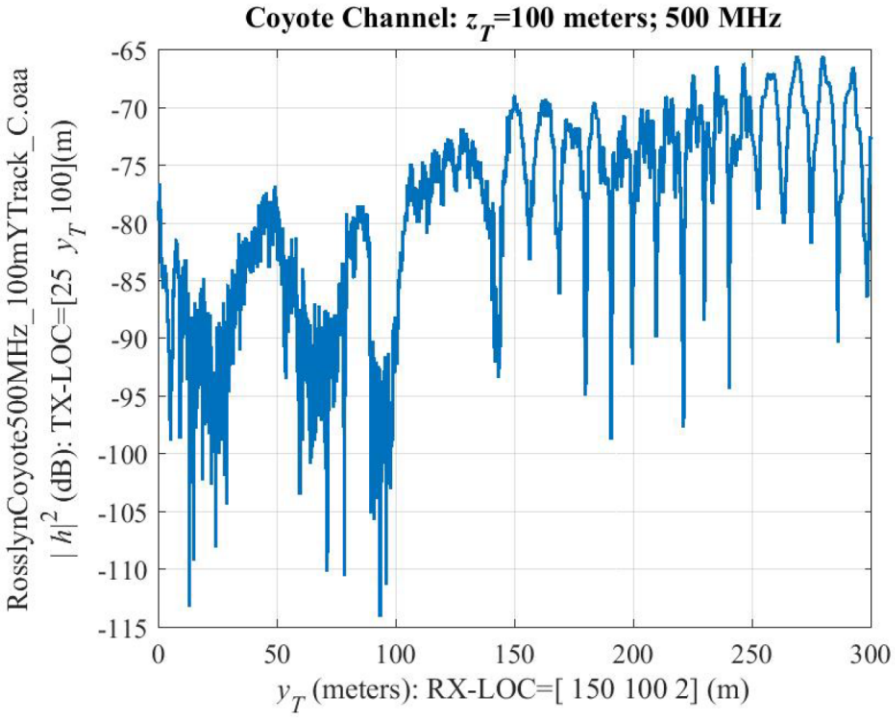

Figure 19. Narrowband channel amplitude from the UAV flying the y-axis track at 100 meters height broadcasting to the street-level receiver.

Figures 20 and 21 "identify" potential fading processes to model these two fading regimes. The heavy shadowing admits Gamma fading [4] whereas the multipath regime admits Weibull, Nakagami, or GEV fading. However, the quotes call out that goodness-of-fit tests are sensitive to both the correlation between samples and outliers. Consequently, a physics-based approach identifying fading processes is always preferred. The forthcoming wideband channel analysis shows that this multipath regime consists of two Rician paths exhibiting fluctuations on the Line-of-Sight (LoS) components. Such generalized Rician processes are an active research area and the resulting models subsume Nakagami, Rician, log-normal, and Hoyt fading [23], [22]. Section 5.3 analyzes the multipath fading in this 100-meter track and verifies that a fluctuating two-ray Rician model produces a good approximation to this fading.

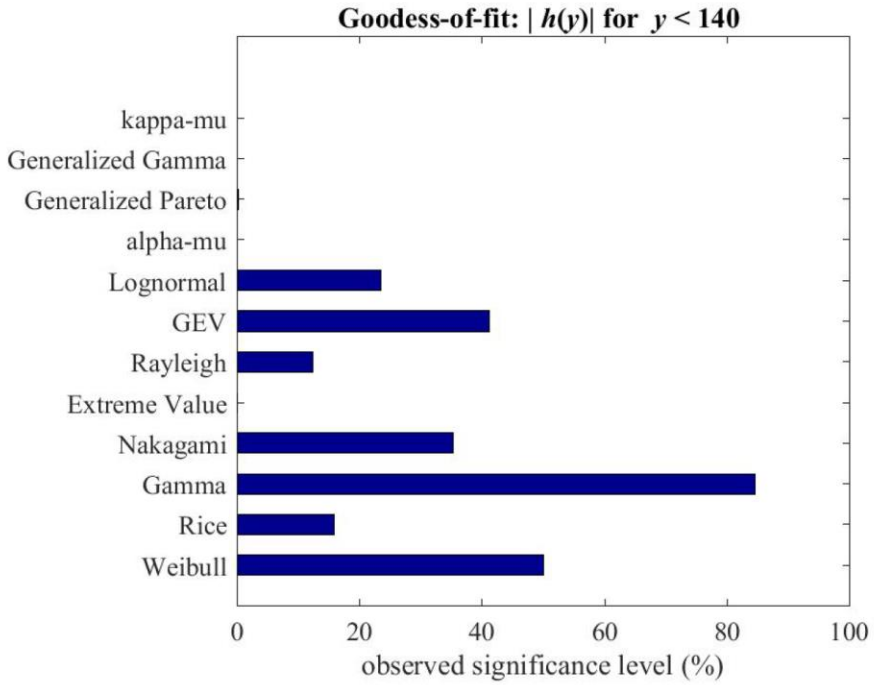

Figure 20. Fading models; shadowing in the first part of the track.

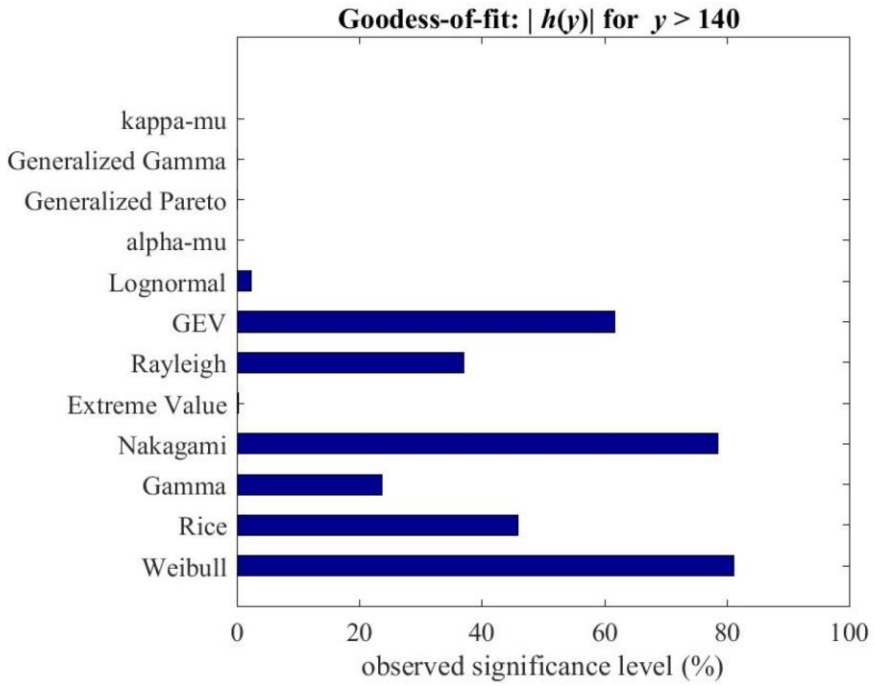

Figure 21. Fading model; multipath in the later part of the track.

5.2 STRAIGHT-LINE TRACKS AT 150 AND 200 METERS HEIGHT

The final simulations move the UAV to greater heights. Figure 22 shows the UAV's channel when flying the y-axis track at $z_T = 150$ (m) height. The multipath fading is still identifiable in the multipath region ($140 < y_T$) whereas the shadowing region ($y_T < 140$) shows multipath in $0 < y_T < 50$. Figure 23 moves the UAV up to $z_T = 200$ (m) height. The multipath fading is still seen in the multipath region but exhibits "fatter" lobes. The shadowing region continues its migration from shadowing to multipath with increasing height. These 100-, 150-, and 200-meter tracks belong to the ensemble of tracks with variable heights. The next section examines such ensembles of tracks to explain these fading regions.

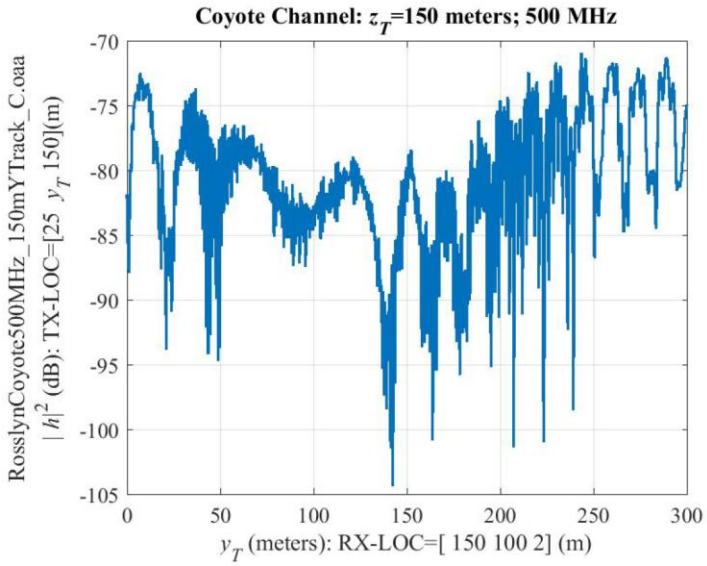

Figure 22. Narrowband channel amplitude from the UAV flying the y-axis at $z_T = 150$ (m) broadcasting to the street-level receiver.

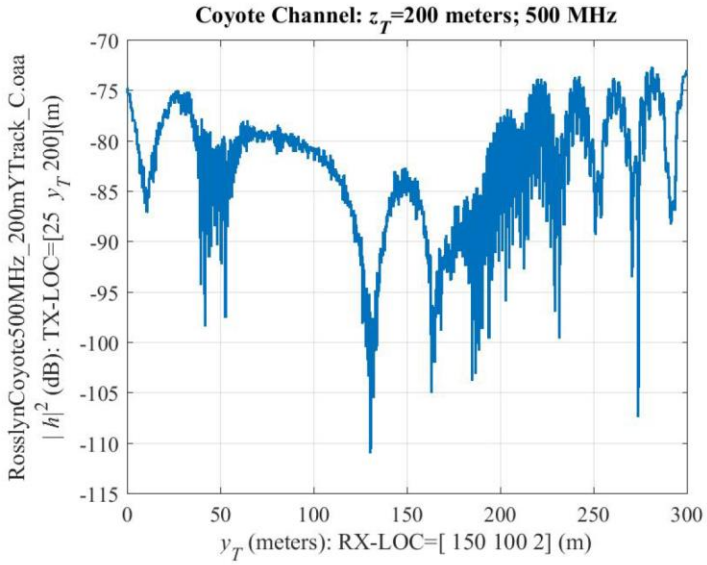

Figure 23. Narrowband channel amplitude from the UAV flying the y-axis track at $z_T = 200$ (m) broadcasting to the street-level receiver.

5.3 FADING SUMMARY

The UAV simulations of the y-axis tracks flying at 100, 150, and 200 meters height reveal two distinct fading regimes:

- heavy shadowing,
- multipath fading.

Figure 24 justifies "multipath" by comparing the multipath fading on the 100-meter track (Figure 19) to a Fluctuating Two-Ray (FTR) fading model of the form

$$h_{\mathrm{FTR}}(y_T) = h_{\mathrm{SLOW}}(y_T) \cdot \{1 + \rho \exp(j2\pi k_P y_T)\} + g(y_T).$$

The slow fading $\{h_{\mathrm{SLOW}}(y_T)\}$ is estimated from the 100-meter track and plotted in both panels for clarity. The FTR model consists of two paths with spatial "Doppler" frequency $k_P \approx 11$ meters, a path ratio $\rho = 0.8$, and a small Gaussian noise $\{g(y_T)\}$ term. Figure 24 shows that this FTR model captures most of the multipath fading. Therefore, developing robust FTR estimators and identifying slow fading processes are recommendations in Section 11.

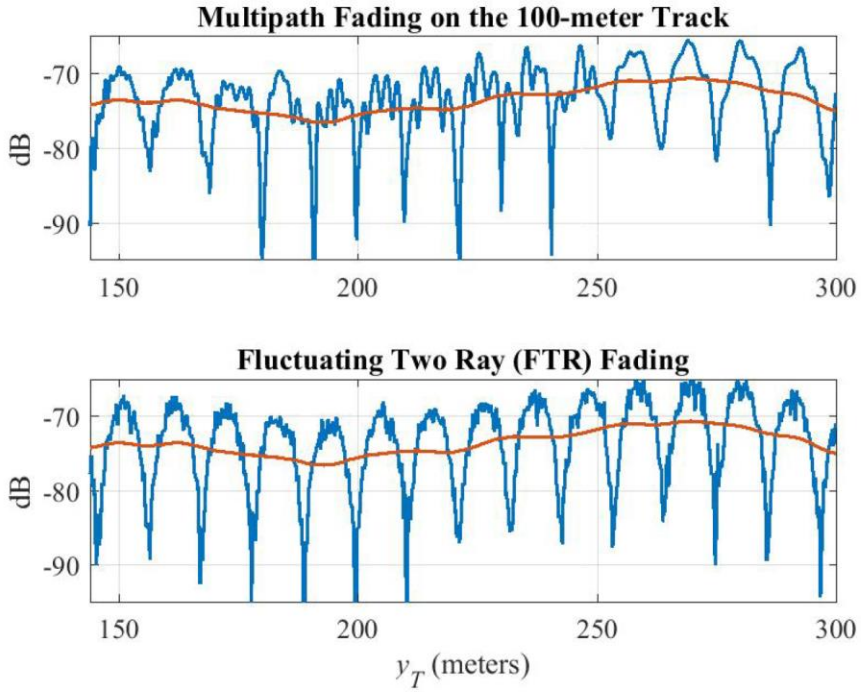

Figure 24. Upper panel: Multipath fading plotted with the slow-fading component. Lower panel: Simulated FTR fading plotted with the slow-fading component.

6. TRACK STRUCTURES IN 2-D VERTICAL SLICES AT 500 MHZ

This section examine vertical "slices" of the narrowband channels to understand how the y-tracks of the preceding section behave as a function of the UAV height. Section 6.1 fixes the street-level receiver and varies the UAV's location over y and z at a fixed downrange distance. These y-z slices are graphical explanations of the fading regimes: buildings cause shadowing; non-shadowed regions exhibit two-ray fading. Section 6.2 moves the slices down range to observe increasing shadowing and slower spatial interference. Section 6.3 reports these findings: (*i*) simple geometry explains how the building's shadows expand as the slices move downrange (*ii*) the non-standard fading is caused by the UAV traveling across the face of an interference ring rather than traversing the rings as is typical for ground-level vehicles.

6.1 VERTICAL SLICE AT $X_T = 25$ METERS

As in the preceding section, the UAV broadcasts from position $\mathbf{r}_T$ through a bottom-mounted 1-inch whip to the street-level receiver at fixed location $\mathbf{r}_R$ equipped with a half-wavelength (0.3 m) vertical dipole. The receiver's location is fixed:

$$\mathbf{r}_R = \begin{bmatrix} x_R \\ y_R \\ z_R \end{bmatrix} = \begin{bmatrix} 150 \\ 200 \\ 2 \end{bmatrix} \quad [\text{m}].$$

The transmitter's location is confined to a y-z "slice":

$$\mathbf{r}_T = \begin{bmatrix} x_T \\ y_T \\ z_T \end{bmatrix} = \begin{bmatrix} 25 \\ y_T \\ z_T \end{bmatrix} \quad [\text{m}].$$

Figure 25 shows the channels in the y-z slice. As in the preceding track simulations, the UAV is aligned with the y-axis and flying level parallel to the y-axis.

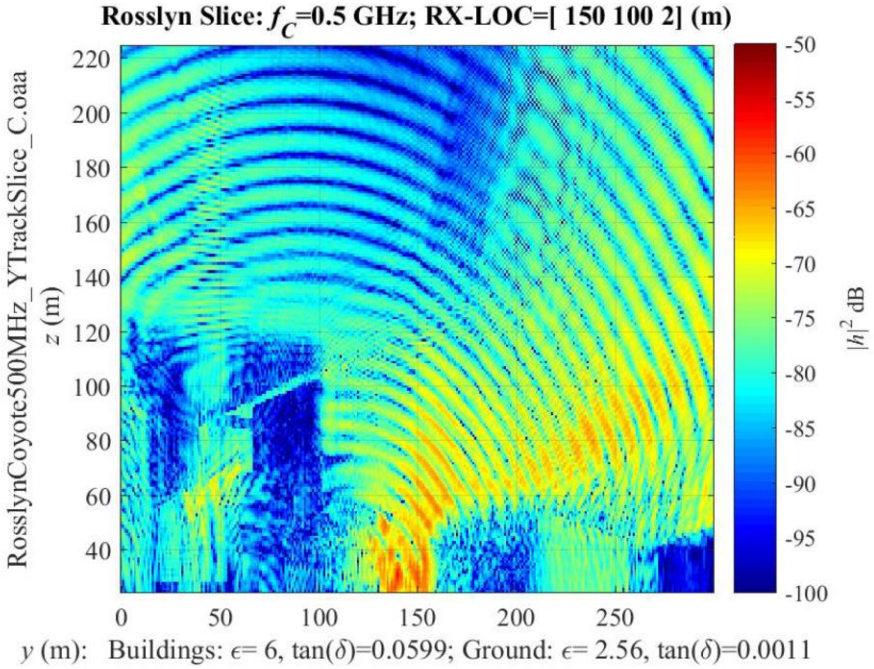

Figure 25. UAV channels at 500-MHz to the street-level receiver; UAV is on the slice at $x = +25$ meters.

Figure 26 puts this slice in the city to orient the UAV channels to the 3-D geometry. The vertical slice explains the fading regions observed along the y-axis tracks of Section 5. The vertical slice shows that buildings cause heavy shadowing in the shadowing region ($y_T < 140$), provided the UAV is below 120 meters. This vertical slice also explains the fading transition to a multipath in the shadowing region with increasing height—the tracks at 150- and 200-meters height are not blocked but traversing a multipath region. In the multipath region ($y_T > 140$), the 100-, 150- and 200-meter tracks are indeed flying through a classic two-ray interference region with the lobes "fattening" with increasing height.

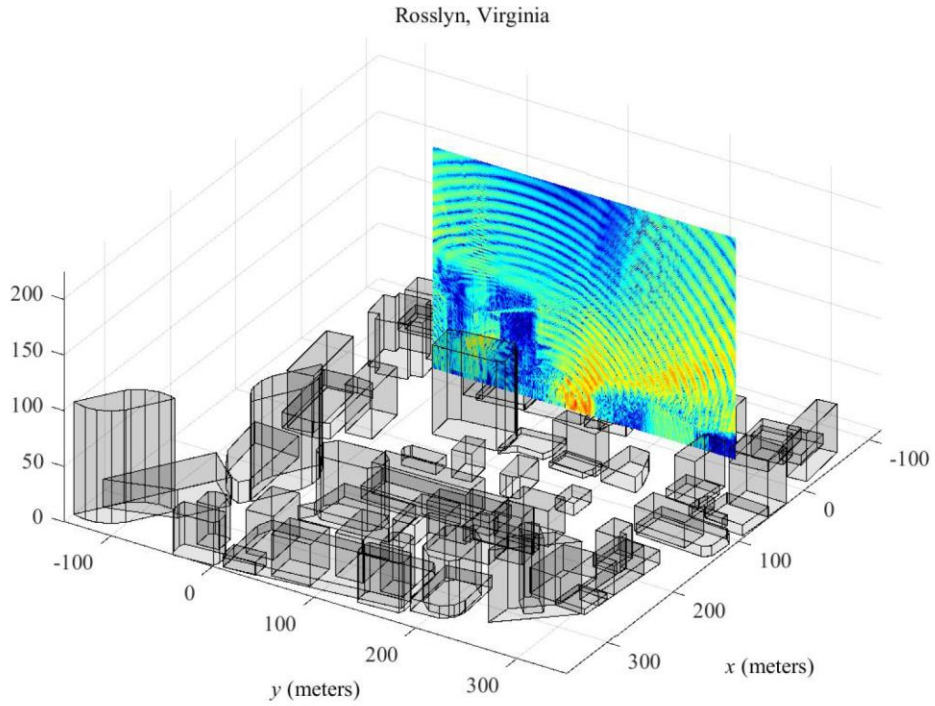

Figure 26. UAV channels at 500-MHz; UAV is on the slice at $x_T = +25$ meters. The street-level receiver is at $x_R = 150$, $y_R = 200$, $z_R = 2$ meters.

6.2 VERTICAL SLICES MOVING DOWNRANGE

The next series of images move the vertical slices further away from the receiver to reveal the effect of shadowing and blockage by the buildings.

Slice at -50 meters: Figure 27 moves the slice down the x-axis to $x_T = -50$ meters. Figure 28 puts this slice in the city's 3-D geometry. The consequence for this move is that the building increases shadowing up to 140 meters in the first part of the track ($y_T < 140$). The interference tends to a circular pattern centered at $y \approx 125$ meters.

Slice at -100 meters: Figure 29 slices the UAV channel at $x_T = -100$ meters. Figure 30 shows that a low building blocks the lower heights while the buildings now shadow the entire first part of the track ($y_T < 140$). The remaining interference still shows the circular pattern centered at $y \approx 150$ with the interference rings getting "fatter" compared to the rings at $x = -50$ meters.

Slice at -200 meters: Figures 31 and 32 slices the UAV channel at $x_T = -200$ meters. The buildings are shadowing the entire first part of the track ($y_T < 140$) and the interference rings are even "fatter" than the previous slices.

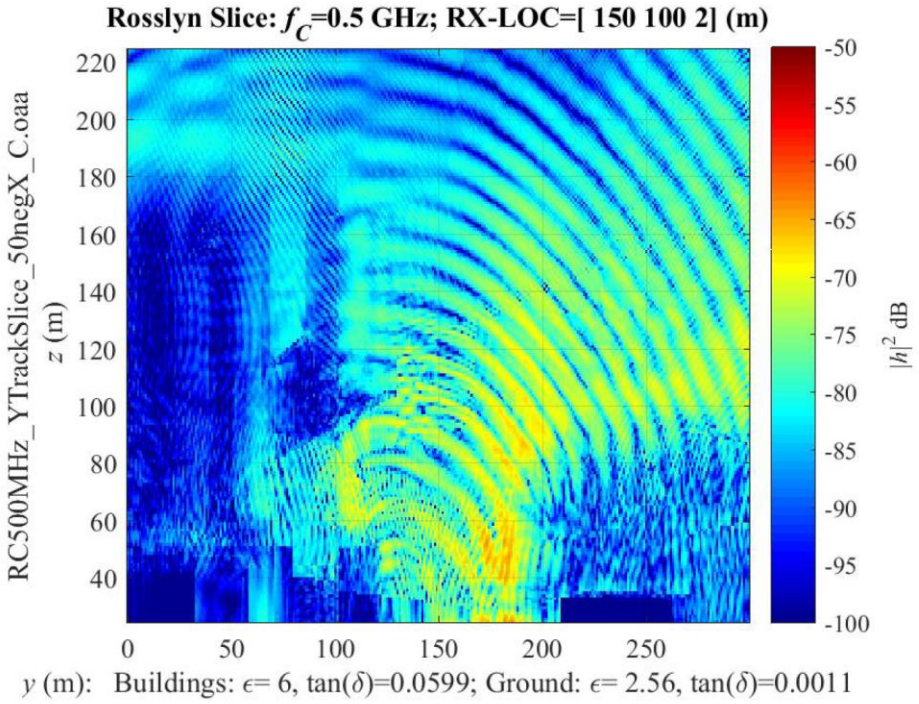

Figure 27. 500-MHz channels from the UAV to the street-level receiver; UAV is on the slice at $x_T = -50$ meters.

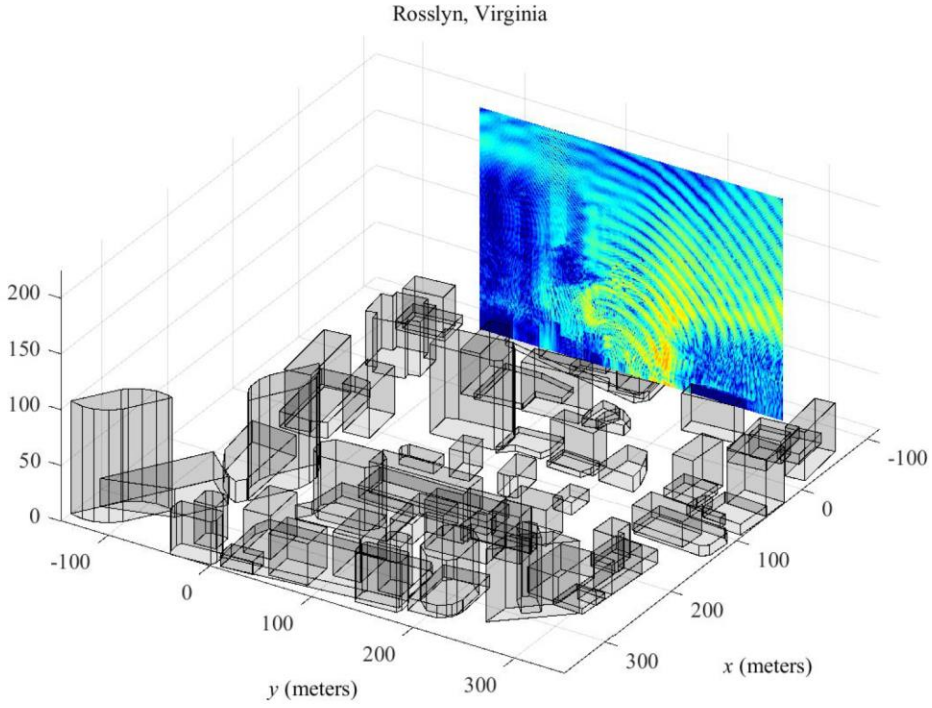

Figure 28. UAV channels at 500 MHz in the 3-D city; UAV is on the slice at $x_T = -50$ meters. Street-level receiver is at $x_R = 150$, $y_R = 200$, $z_R = 2$ meters.

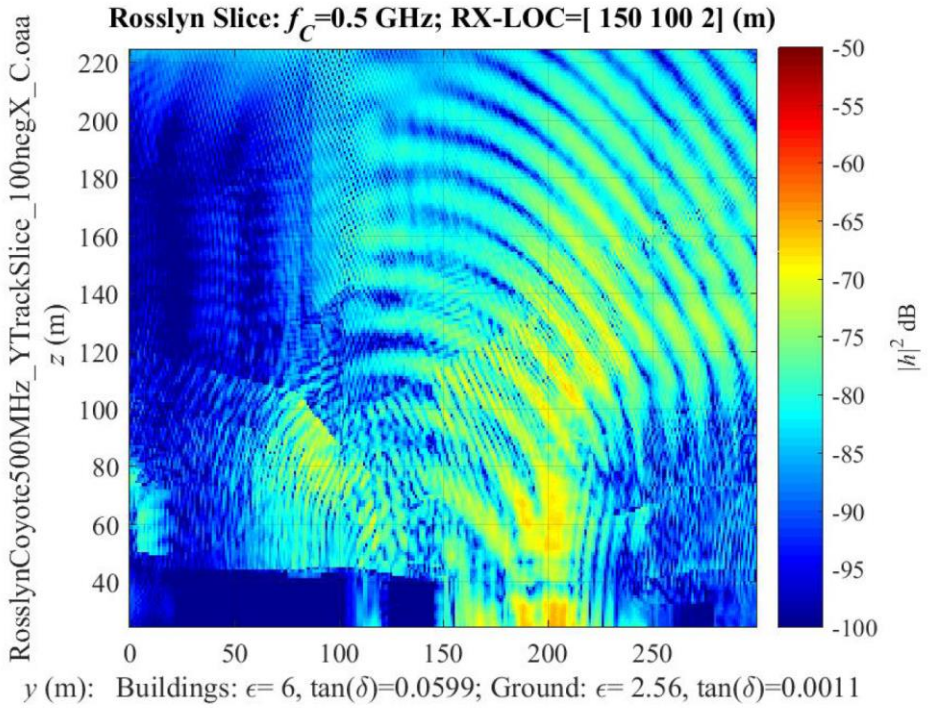

Figure 29. UAV channels at 500 MHz to the street-level receiver; UAV is on the slice at $x_T = -100$ meters. Street-level receiver is at $x_R = 150$, $y_R = 200$, $z_R = 2$ meters.

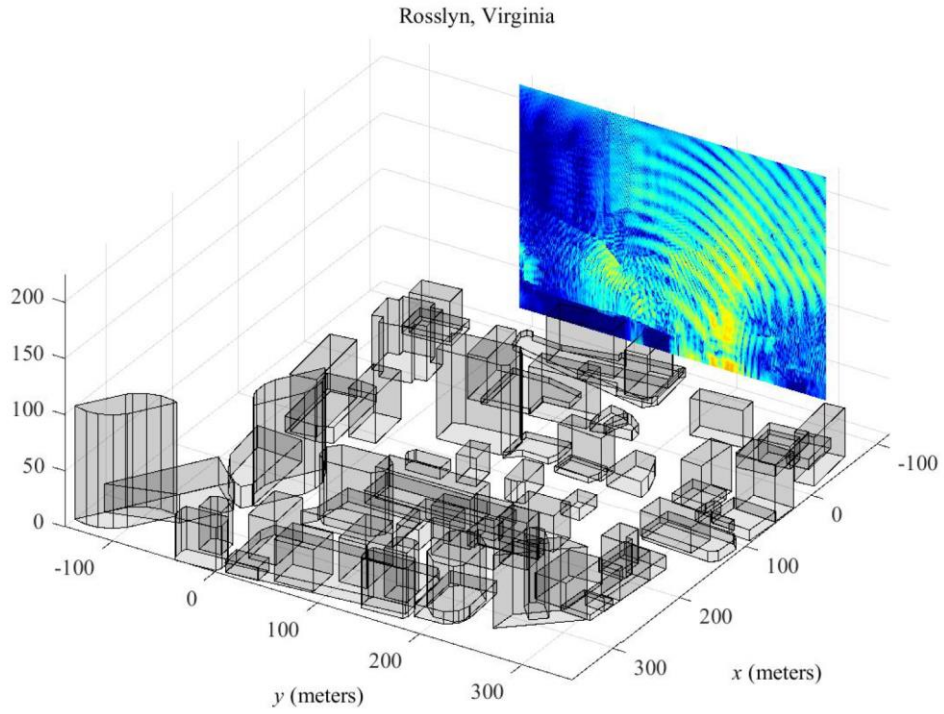

Figure 30. UAV channels at 500 MHz in the 3-D city; UAV is on the slice at $x_T = -100$ meters. Street-level receiver is at $x_R = 150$, $y_R = 200$, $z_R = 2$ meters.

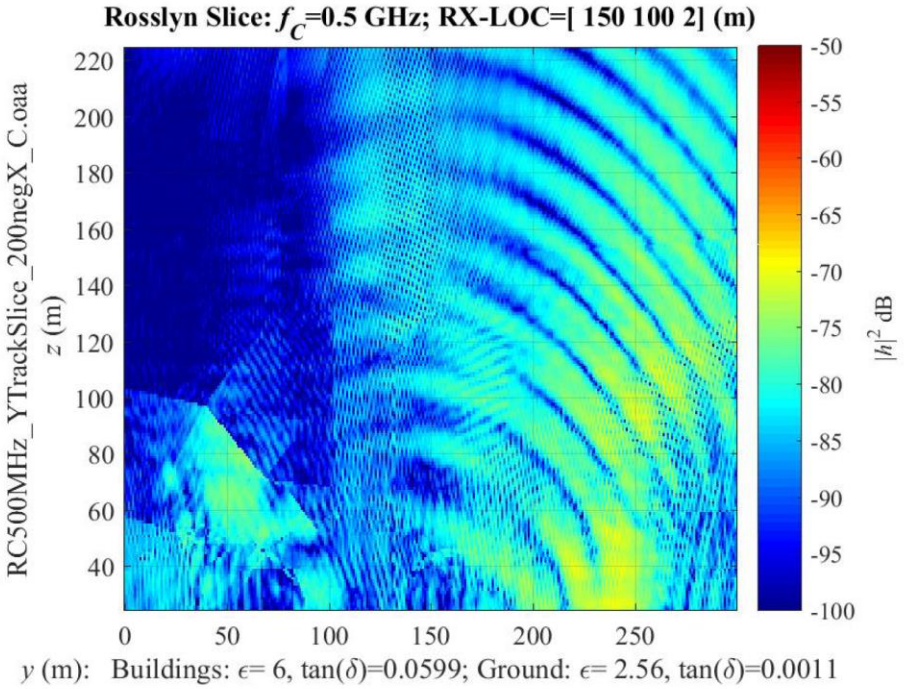

Figure 31. UAV channels at 500 MHz to the street-level receiver; sliced at $x_T = -200$ meters.

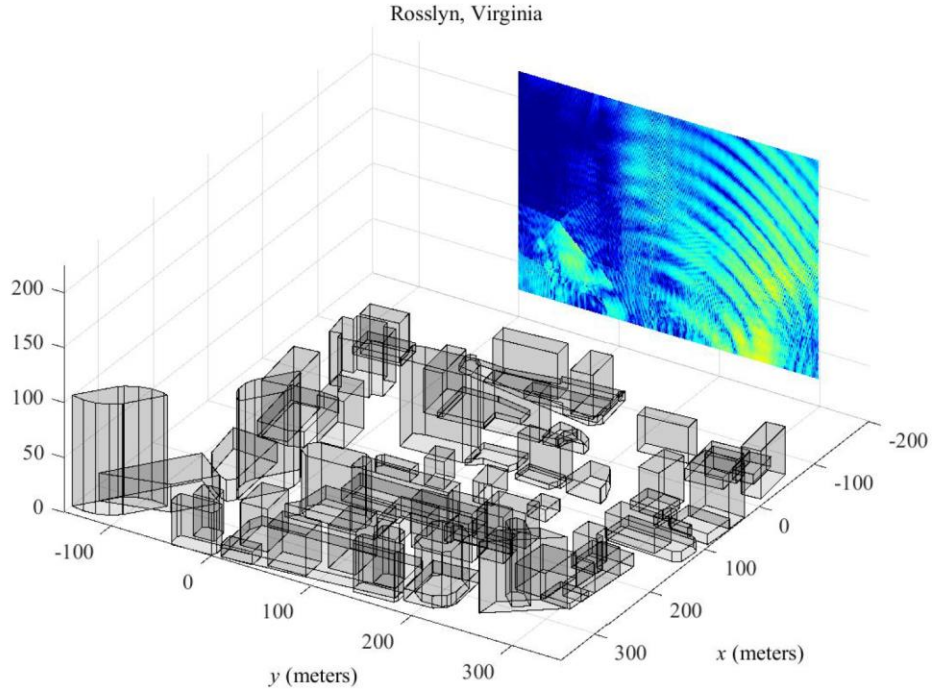

Figure 32. UAV channels at 500 MHz in the 3-D city; UAV in on the slice at $x_T = -200$ meters. Street-level receiver is at $x_R = 150$, $y_R = 200$, $z_R = 2$ meters.

6.3 FADING ANALYSIS

Figure 33 illustrates the associated shadow geometry. For a ground-level receiver located a distance d_B from a building with height h_B, that building's shadow height h_A increases linearly as the distance d_A increases from the building:

$$h_A = (d_A + d_B)\frac{h_B}{d_B}.$$

This simple shadow geometry explains the growing shadows cast by the several buildings as the slices move down range.

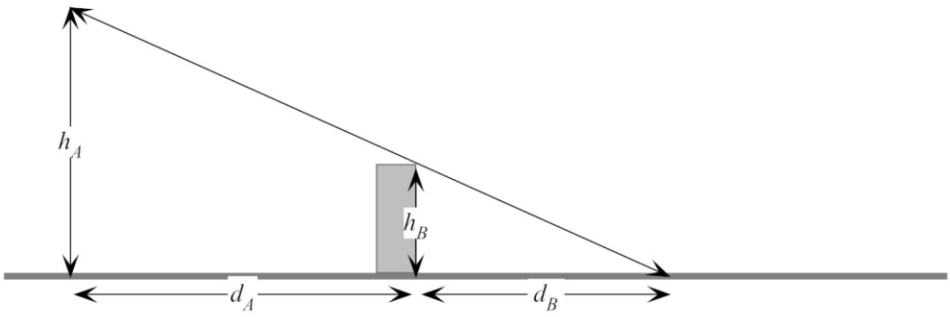

Figure 33. UAV shadowing geometry.

The slices also explain the multi-mode nature of the narrowband fading observed in Section 5 that varied with UAV height:

F-1 Increasing UAV height transitions the fading from shadowing to multipath.

F-2 The rapid switching between fading regions is caused by the UAV flying across shadowing regions.

F-3 The multipath regions exhibit classic two-ray interference.

Consequently, F-1 identifies the city's buildings as causing the heavy shadowing. This identification points to physics-based fading models in these regions, such as the recent advances in the Gamma distribution [2], [4], [26]. F-2 points out that the rapid switching between fading regions requires the radios to adapt to this switching. F-3 identifies classic two-ray interference pattern in the multipath region. The twist is that the observed non-standard interference is caused by the UAV traveling across the face of an interference ring rather than traversing the rings that are typical for ground-level vehicles.

Up to now, the UAV channels are narrowband. The next section examines wideband UAV channels. The finding is that the narrowband fading is caused multiple paths observed in the wideband delay spread function.

7. WIDEBAND TRACKS AT 500 MHZ

Wideband channels reveal additional insights into the fading along the UAV tracks. The two fading regimes—heavy shadowing and multipath fading— are displayed in the spectral plots of the channel. Bringing these channels into the time domain reveals the multipath and the fading. Section 7.1 reports on the wideband fading for the UAV flying a straight-line track at 100 meters height. At this height, the channel splits into two paths: the multipath region shows fast fading on two paths; the heavy shadowing region shows slower fading on one path. Section 7.2 raises the track height to 200 meters. This height puts the track into multipath region with relatively slow fading on two paths. Section 7.3 observes that the narrow-band fading regimes are present in these wideband channels.

7.1 WIDBAND TRACKS AT 100-METER HEIGHT

The UAV broadcasts from position $\mathbf{r}_T$ through a bottom-mounted 1-inch whip to the street-level receiver at fixed location $\mathbf{r}_R$ equipped with a half-wavelength (0.3 m) vertical dipole:

$$\mathbf{r}_T(y_T) = \begin{bmatrix} x_T \\ y_T \\ z_T \end{bmatrix} = \begin{bmatrix} 25 \\ y_T \\ 100 \end{bmatrix}; \quad \mathbf{r}_R = \begin{bmatrix} x_R \\ y_R \\ z_R \end{bmatrix} = \begin{bmatrix} 150 \\ 200 \\ 2 \end{bmatrix} \quad [\text{m}].$$

Figure 34 displays the wideband channel as the UAV travels along the 100-meter track and transmits to the street-level receiver.

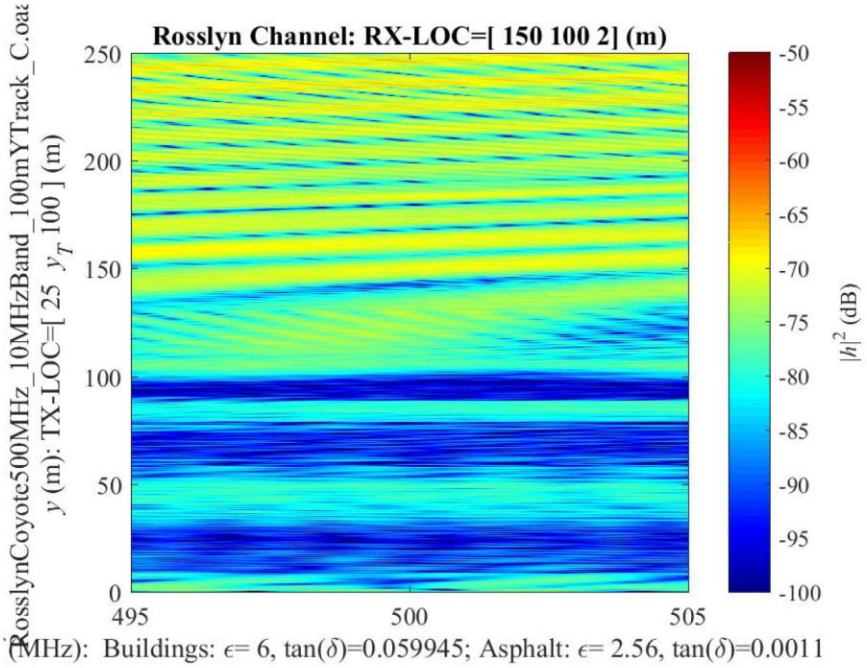

Figure 34. The 10-MHz channel centered on 500 MHz; UAV on the track at 100-meter height broadcasting to the street-level receiver.

The figure displays the channel as a function of UAV position y_T and frequency f:

$$|\widehat{h}(f; \mathbf{r}_T(y_T), \mathbf{r}_R)|^2 \quad [\text{dB}]$$

and is analogous to the *time-varying transfer function* [5]. The "hat" denotes the Fourier transform

$$\widehat{h}(f; \mathbf{r}_T(y_T), \mathbf{r}_R) = \int_{-\infty}^{\infty} e^{-j2\pi f\tau} h(\tau; \mathbf{r}_T(y_T), \mathbf{r}_R) d\tau,$$

where $h(\tau; \mathbf{r}_T(y_T), \mathbf{r}_R)$ is the spatial analog of the delay spread function of Equation 6.

Context for this figure is found in two preceding plots. Figure 19 shows the narrowband fading at 500 MHz. Figure 25 is the associated 2-D slice showing the initial portion of the track is shadowed by the buildings while the remainder of the track is well modeled by two-ray fading:

- heavy shadowing: $0 \leq y_T \leq 100$ [m]
- multipath fading $150 \leq y_T \leq 200$ [m]

Figure 34 extends these narrowband slices to a 10-MHz bandwidth to reveal the fading in the heavy shadowing region is almost independent of frequency whereas the multipath region shows that the fading varies with frequency. Pulling this wideband channel into the time domain makes explicit the fading in these two regions.

Estimating a *delay spread function* from a *bandlimited* observation of its spatially varying transfer function requires windowing the inverse Fourier transform:

$$h(\tau; \mathbf{r}_T, \mathbf{r}_R) = \int_{-\infty}^{\infty} e^{+j2\pi f\tau} \widehat{h}(f; \mathbf{r}_T, \mathbf{r}_R) \widehat{w}(f) df.$$

This report employs Gaussian windows:

$$w(t) = \frac{1}{t_G} \exp\left(-\pi \frac{t^2}{t_G^2}\right)$$

where the scaling in the time domain is rigged for unit area:

$$1 = \int_{-\infty}^{\infty} w(t) dt.$$

If the channel is to deliver a time resolution Δt at level w_0 defined as

$$w_0 = t_G w(\Delta t/2),$$

the time spread t_G is set at

$$t_G = \frac{\Delta t}{2} \sqrt{\frac{-\pi}{\log(w_0)}}.$$

The next two figures estimate the delay spread function using time resolutions of $\Delta t = 1$ and 0.5 μs. The wideband channel shows that there are two paths hidden in the fading.

Figure 35 shows the delay spread estimate with the time resolution $\Delta t = 1$ μs for $w_0 = -20$ dB. The estimate shows one path at $\tau_1 \approx 0.8$ μs. This path attenuates in the heavy fading region ($0 < y_T < 100$ meters) but is the dominate path in the the multipath region ($100 < y_T < 250$ meters). The estimate also shows a weaker second path with variable delay: $0.8 < \tau_2(y_T) < 1.5$ μs. Increasing the time resolution provides finer detail of the two paths.

Figure 36 employs $\Delta t = 0.5$ μs resolution while still using $w_0 = -20$ dB. The delay spread function shows the two paths with finer delay resolution: the strong path at $\tau_1 = 0.8$ μs delay; the weaker path with time-varying delay now resolved to $1.0 < \tau_2(y_T) < 1.5$ μs. The closest model in the literature to this fading is the Fluctuating Two-Ray (FTR) fading [22]. The heavy shadowing region reduces the magnitude of both paths and slows the fade rate of both paths. These observations are consistent with the narrowband channels of Section 5.1.

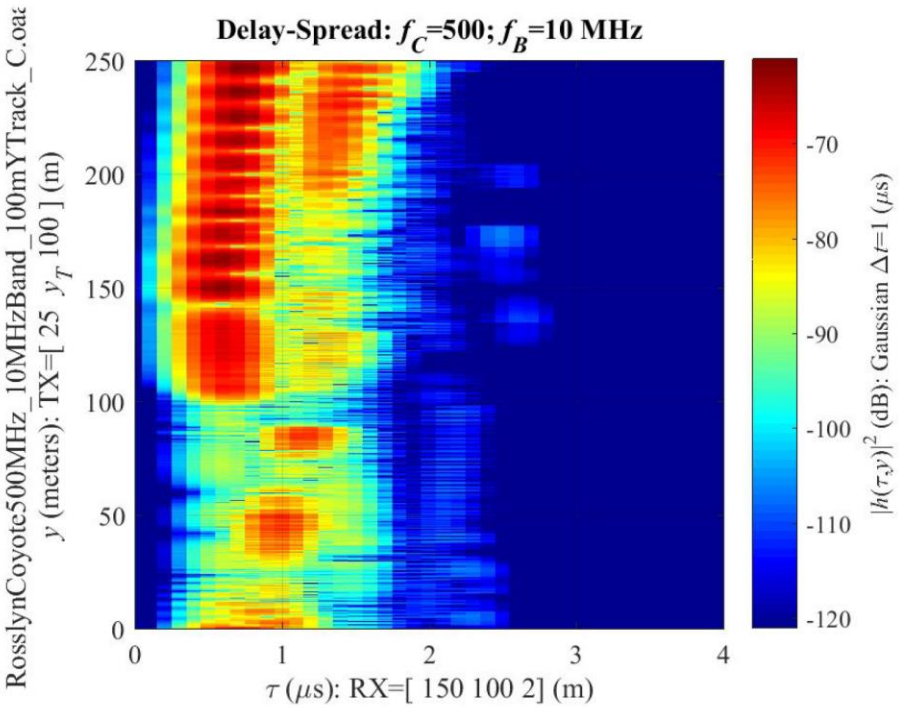

Figure 35. Delay spread estimate of the 10-MHz channel centered on 500 MHz; UAV on the track at 100-meter height broadcasting to the street-level receiver; Gaussian window with 1-μs resolution.

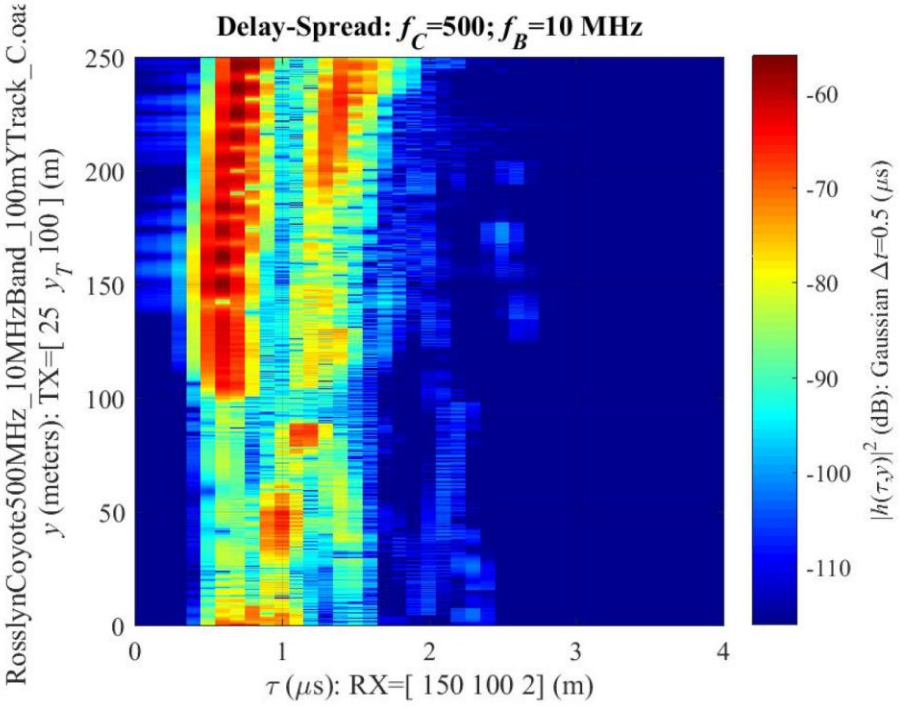

Figure 36. Delay spread estimate of the 10-MHz channel centered on 500 MHz; UAV on the track at 100-meter height broadcasting to the street-level receiver; Gaussian window with 0.5-μs resolution.

7.2 WIDBAND TRACKS AT 200-METER HEIGHT

Figure 37 shows the wideband spatially varying transfer function plotted over a 10-MHz band centered on 500 MHz as the UAV flies the y-track at 200 meters height. Two preceding plots provide explain the slowly varying interference pattern. Figure 23 shows the narrowband interference at 500 MHz. Figure 25 is the associated 2-D slice showing that the y-track at 200 meters is lifts the UAV out of the shadowing by the buildings—the wideband channel is only registering two-path interference.

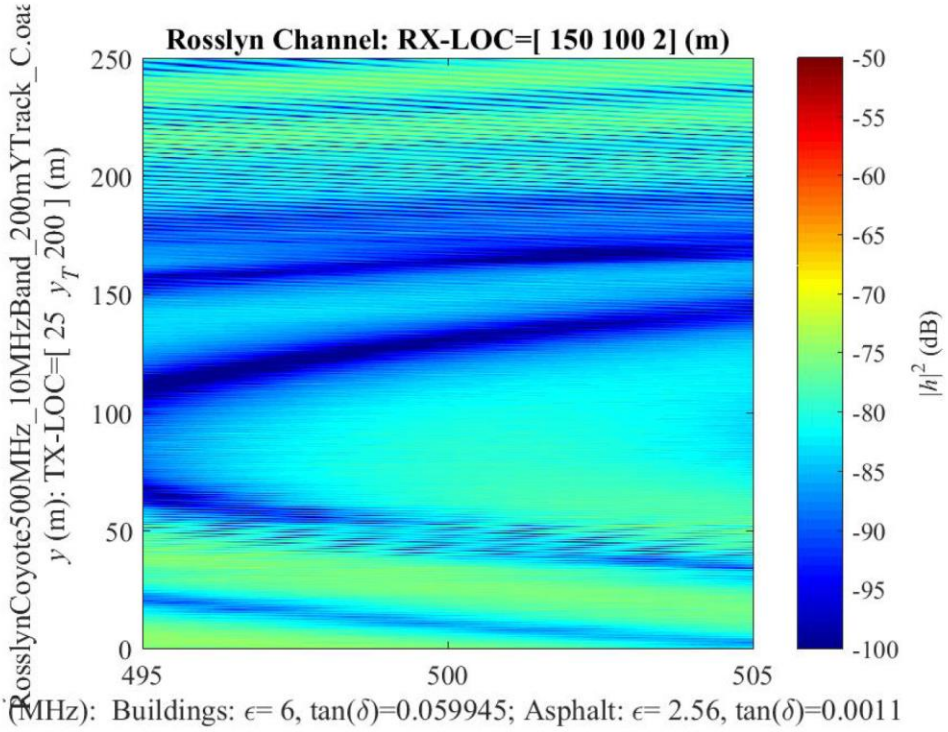

Figure 37. The 10-MHz channel centered on 500 MHz; UAV on the track at 200-meter height broadcasting to the street-level receiver.

Figure 38 estimates the delay spread function using the 0.5-μs window. This figure shows the fading consists of a strong path at nearly constant delay of 0.8 μs and a weaker path with delay varying from 1.0 to 1.5 μs. This weaker path consists of two sub paths in $0 < y_T < 90$ meters that merge into a single path. Because this second path is substantially weaker than the first path, this three-path modeling is not significant for this channel modeling. What is significant is that there are two paths and that the FTR fading is still a credible fading model. Therefore, development and application of FTR fading is a recommendation called out in Section 11. Other windows, such as the Kaiser window [12], provide different tradeoffs for delay spread estimation. Assessing windows a lower priority and not included in the recommendations of Section 11.

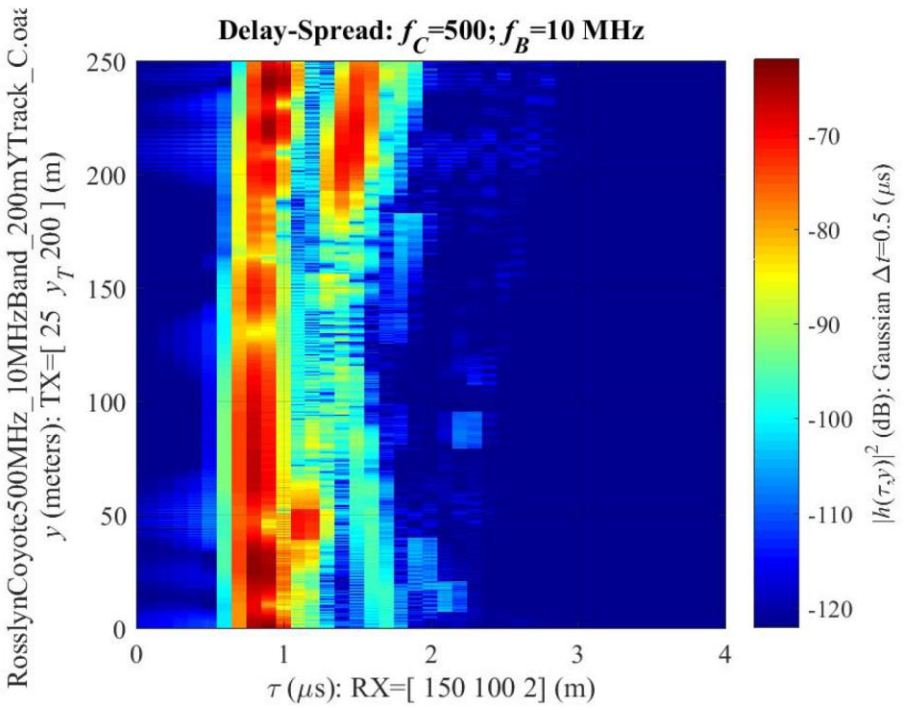

Figure 38. Delay spread estimate of the 10-MHz channel centered on 500 MHz; UAV on the track at 200-meter height broadcasting to the street-level receiver; Gaussian window with 0.5-μs resolution.

7.3 WIDEBAND CHANNEL SUMMARY

The extra bandwidth of these wideband channel simulations reveal that multiple paths underlie the fading observed in the narrowband channel simulations. For example, the narrowband simulations of the UAV flying the y-track at 100 meter height show an interference pattern characteristic of two paths in Figure 19. This narrowband fading conjecture is verified by the wideband simulation that does show two paths in Figure 36. The payoff of these wideband simulations is:

- Verification of the paths in the multipath and heavy shadowing regions,
- Verification that some paths have time-varying delays $\tau_\ell(t)$.

This verification of the multiple paths simplifies the channel modeling—the fading of the narrowband channels is representative of the wideband channels up to 10 MHz. Therefore, the remainder of this report employs the narrowband channel.

This page is intentionally left blank

8. UAV AS A RELAY

This section assesses the performance shift that a UAV relay delivers over direct ground-to-ground communication. Figure 39 illustrates the two-node simulation. Node 1 and Node 2 are located at $\mathbf{r}_1$ and $\mathbf{r}_2$, respectively. These street-level nodes operate at at 500 MHz through half-wavelength (0.3 m) vertical dipoles. Section 8.1 computes the ground-to-ground channel between Node 1 and Node 2. There is no line-of-sight—the channel between the two nodes consists of multiple rays that arrive by reflections and diffractions. Section 8.2 computes the UAV-relay channels connecting both nodes when the UAV operates at 150 meters height. Section 8.3 compares the ground-to-ground channel to the UAV-relay channels. The payoff is that the UAV-relay delivers five times throughput over the ground-to-ground channel at 1 Watt total power. The UAV-relay still delivers over three times throughput at 0.1 Watt total power. Assessing throughput as a function of UAV height and linking to the city's average geometry is an ongoing investigation.

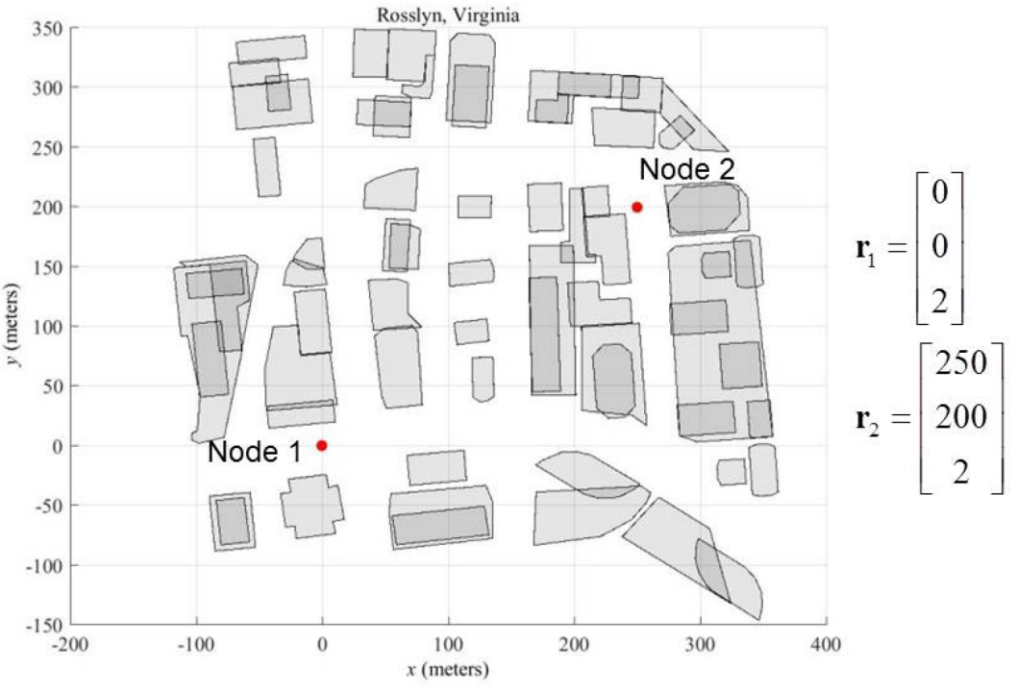

Figure 39. Top view of Node 1 and Node 2.

8.1 GROUND-TO-GROUND CHANNELS

The narrowband channel linking Node 1 and Node 2 at $f_C = 500$ MHz is computed by NEC-BSC to have gain

$$|h(f_C; \mathbf{r}_1, \mathbf{r}_2)|^2 = -115 \quad [\text{dB}].$$

The flat external urban noise model across a $f_B = 1$ MHz band is [13]:

$$p_N = -121 \quad [\text{dBW}].$$

This external noise is distinct from the internal radio noise. By using only this external noise rather than the summing both the external and internal noise, the resulting SNR estimates are upper bounds. The performance shifts of the SNR arise from differences in the signal models and not the noise model. Therefore, using the external noise model is sufficient for this report. Figure 40 plots an upper bound on the link's throughput [10, Equation 4.1]

$$R_b = f_B \log_2 \left(1 + \frac{p_T}{p_N}|h|^2\right)$$

as a function of transmit power for fixed noise p_N and channel $|h|^2$. This plot benchmarks the UAV relay channel between these two nodes.

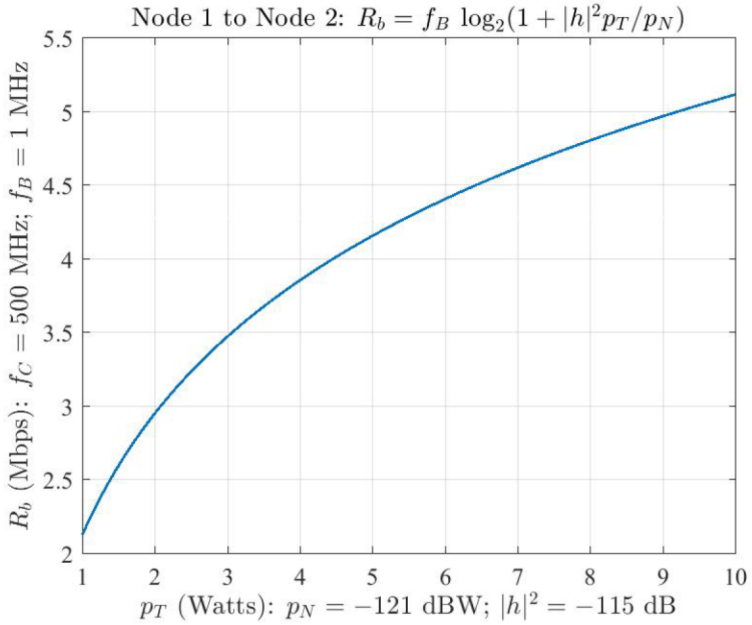

Figure 40. Throughput versus power for the ground-to-ground link between Nodes 1 and 2.

8.2 GROUND-TO-UAV

Figure 41 shows the channels from each node to the UAV operating at 150 meters height. In both channels, there is a null directly over each ground node caused by their vertical antennas. The average Node-to-UAV channel over this region is approximately -84 dB. The ground-to-ground link has a gain of -115 dB. Although relay systems can exploit this 30-dB difference, especially by reducing RF emissions from the nodes, not all UAV positions deliver this gain.

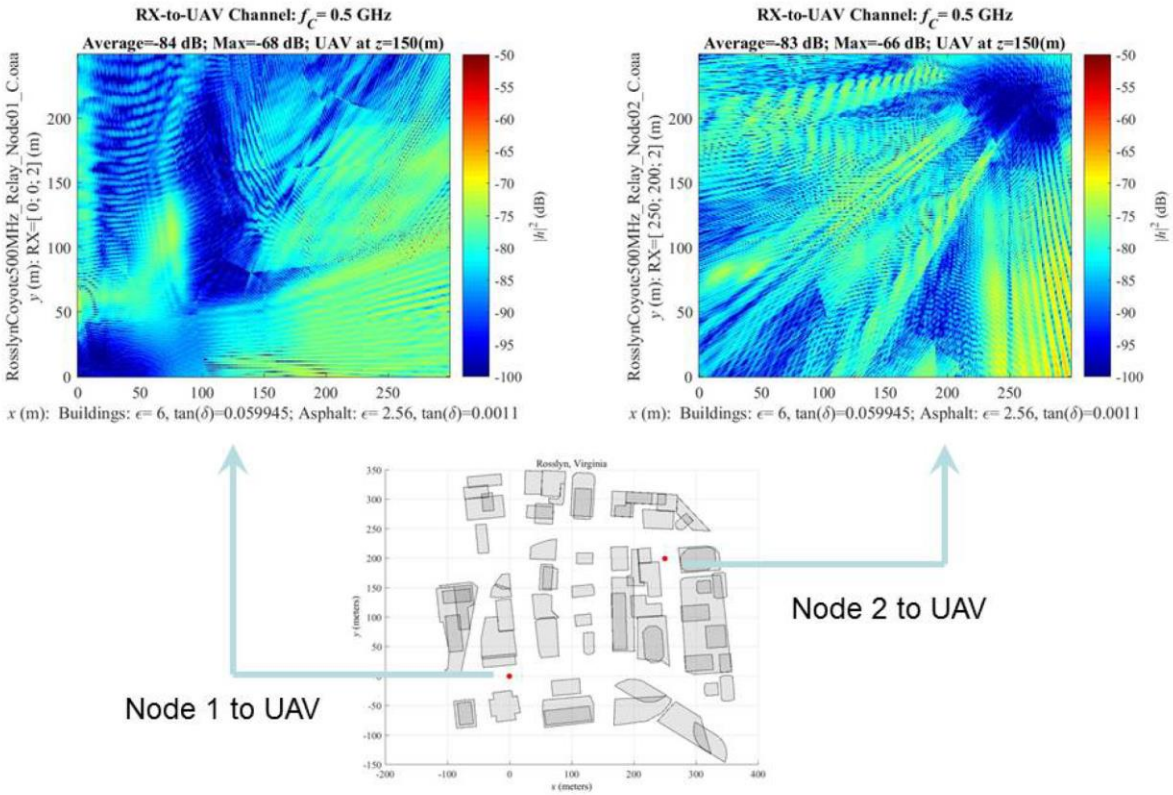

Figure 41. Node-to-UAV channels at 500 MHz.

Figure 42 is a "worst case" for employing the UAV as a relay between the two nodes. This coverage plot is generated by plotting the weakest channel in the two coverage plots of Figure 41. For example, each coverage plot show the nulls caused by the vertical antennas are visible at both nodes. Figure 42 shows both nulls providing verification of "worst case". This plot provides a lower bound on relay performance by requiring the up- and down-links to overcome the worst channel. Figure 43 is a histogram of these worst channels. Most channels center around -88 dB but there is a relatively long tail down to -120 dB. Although ground-to-ground channel has gain -115 dB, 79% of the worst-case channel exceed -95 dB. Comparison of the average throughput clarifies the performance shift this UAV relay delivers.

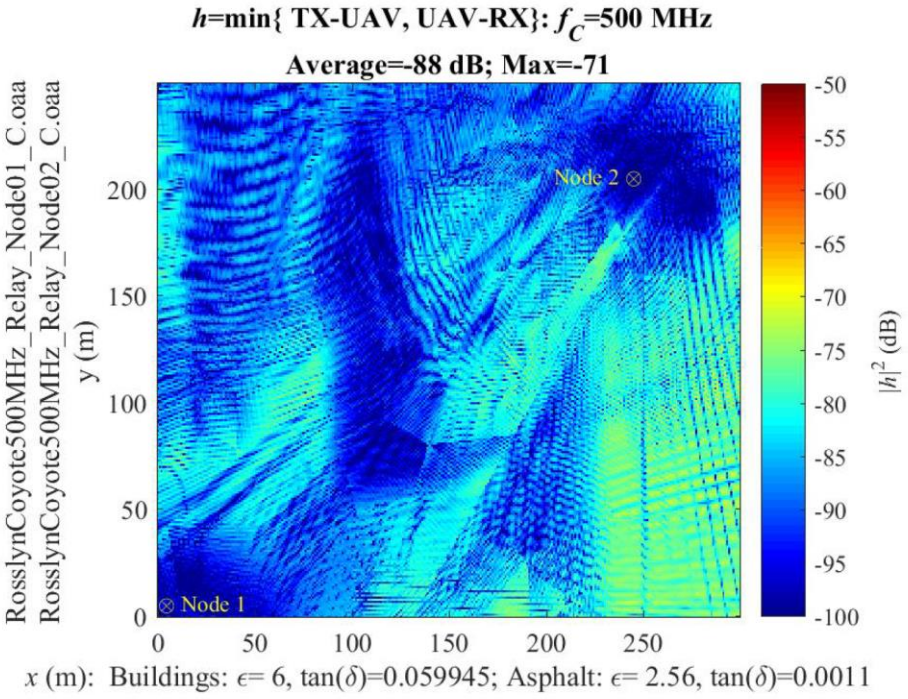

Figure 42. The worst Node-to-UAV channel at 500 MHz.

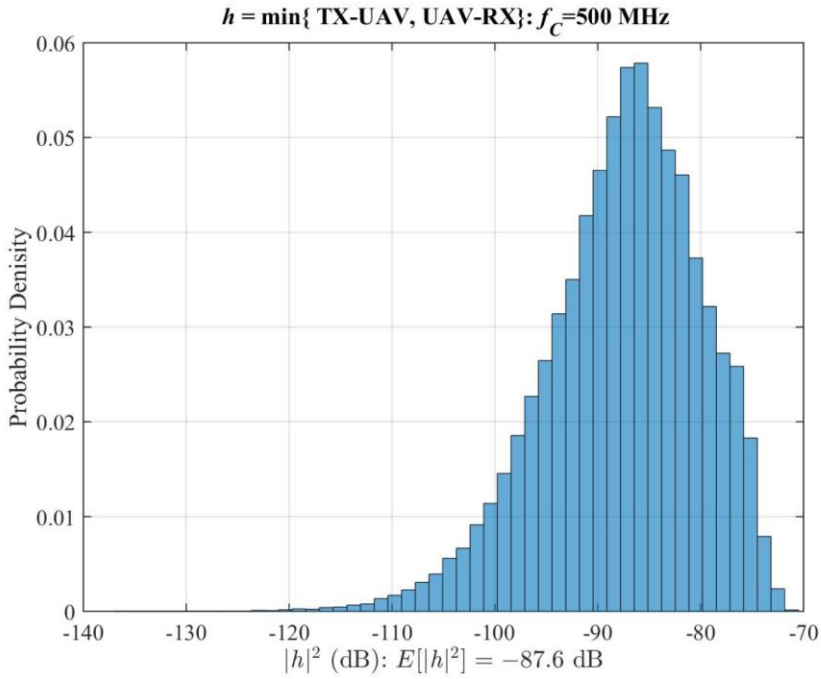

Figure 43. Histogram of the worst Node-to-UAV channels at 500 MHz; UAV flies at 150 m.

8.3 PERFORMANCE SHIFT DELIVERED BY THE UAV RELAY

Any relay scheme assumes wireless power control, even if the power allocation is set at the outset. A simple power allocation equally divides the total relay power p_Σ between the transmitting node's power p_T and the UAV's transmitting $p_{\rm UAV}$:

$$p_\Sigma = p_T + p_{\rm UAV}; \quad p_T, p_{\rm UAV} = p_\Sigma/2.$$

The associated Shannon rate for this UAV relay—not accounting for latency—is computed at each UAV position as

$$R_b(\mathbf{r}_{\rm UAV}) = f_B \cdot \log_2\left(1 + |h_{\rm MIN}(\mathbf{r}_{\rm UAV})|^2 \frac{p_\Sigma/2}{p_N}\right) \quad \text{[Mbps]}.$$

Figures 44 and 45 are the histograms of this Shannon rate for total relay power $p_\Sigma = 1$ and 0.1 Watts using the same bandwidth and noise as the ground-to-ground link in Figure 40. The ground-to-ground link delivers approximately 2.1 Mbps at 1 Watt. The UAV relay rate using $p_\Sigma = 1$ Watt, (equivalently, 0.5 Watts between the ground nodes and the UAV) shows an average rate of approximately 10 Mbps with only a small fraction of the links failing to deliver more than 0.5 Mbps. Reducing the power to $p_\Sigma = 0.1$ Watts still shows an average rate of approximately 7 Mbps and a relatively small fraction of the links delivering less the 2.1 Mbps on on the ground-to-ground link.

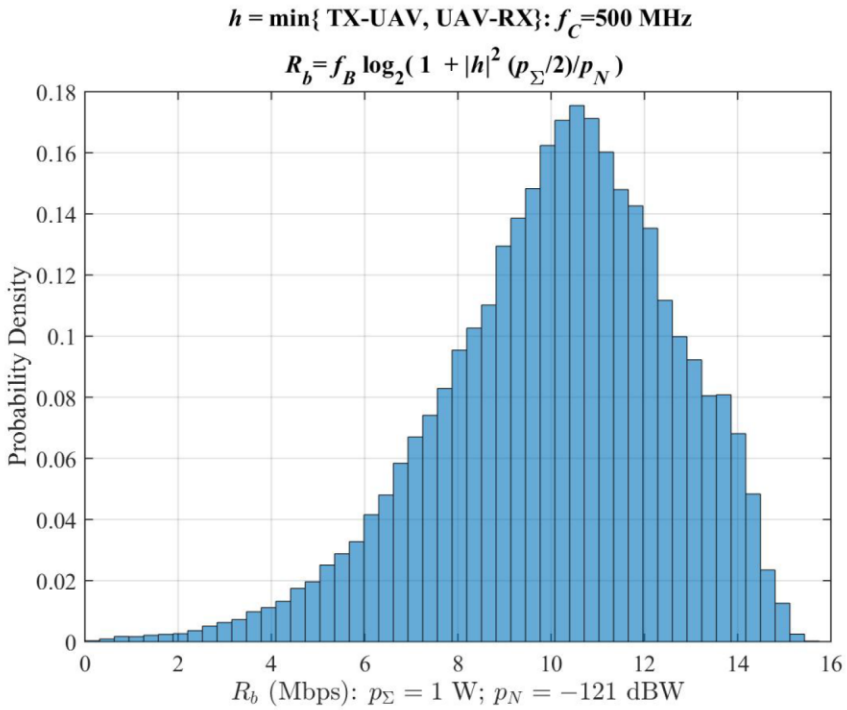

Figure 44. Relay rate; UAV at $z_T = 150$ (m) height; $f_B = 1$ MHz; $p_\Sigma = 1$ Watt.

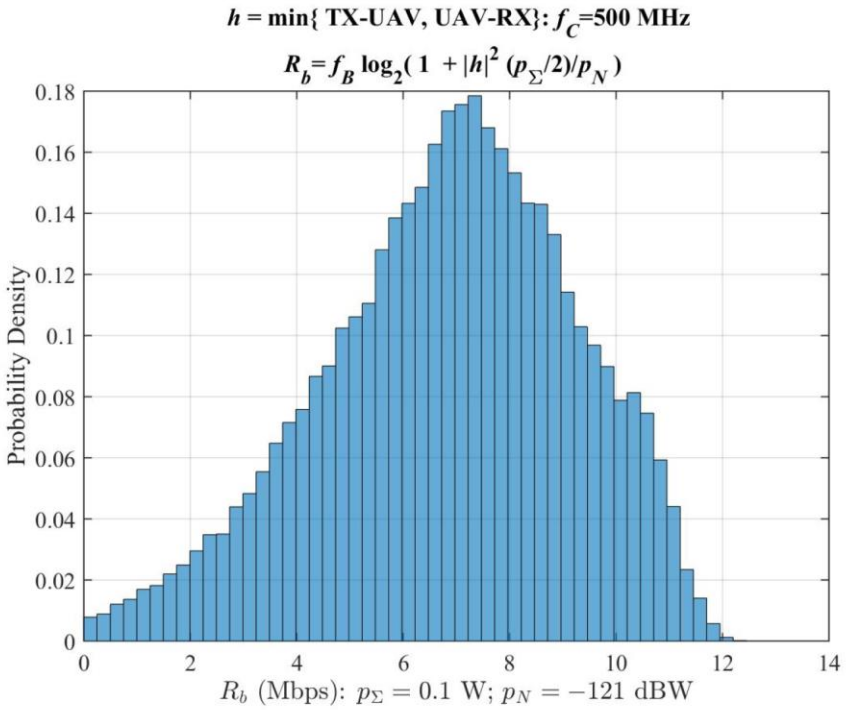

Figure 45. Relay rate; UAV at $z_T = 150$ (m) height; $f_B = 1$ MHz; $p_\Sigma = 0.1$ Watt.

9. CIRCULAR TRACKS

Flying the UAV around a circular track illustrates the opportunities afforded by UAV "loitering" schemes. Section 9.1 sets out the geometry of the circular track and the street-level receiver. Section 9.2 flies the UAV around circular track: the wings are level and the antenna is vertical. The fading exhibits deep nulls but is periodic. This periodic fading could be "learned" by a smart radio to manage throughput. Section 9.3 flies the UAV around the circular track rolled at $45°$. The fading exhibits still exhibits deep nulls but pointing the main load of the UAV's antenna into the city raises the overall gain by 10 dB. Both sections show opportunities to boost throughput.

9.1 CIRCULAR TRACK AT 200 METERS

Figure 46 is a 3-D view of the city and the circular track of the UAV. The circular track is 400 meters in diameter, raised to a height of 200 meters, and centered on $\mathbf{r}_0 = [100,\ 100,\ 200]^{\mathsf{T}}$ meters. The circular track is parameterized by the azimuth angle ϕ measured from $\mathbf{r}_0$:

$$\mathbf{r}_T(\phi) = \begin{bmatrix} 100 \\ 100 \\ 200 \end{bmatrix} + 200 \begin{bmatrix} \cos(\phi) \\ \sin(\phi) \\ 0 \end{bmatrix} \quad [\mathrm{m}].$$

The UAV broadcasts to a street-level receiver fixed at $x_R = 150$, $y_R = 100$ meters. Figure 47 is a top view of this geometry clarifying relation between the circular track and the street-level receiver.

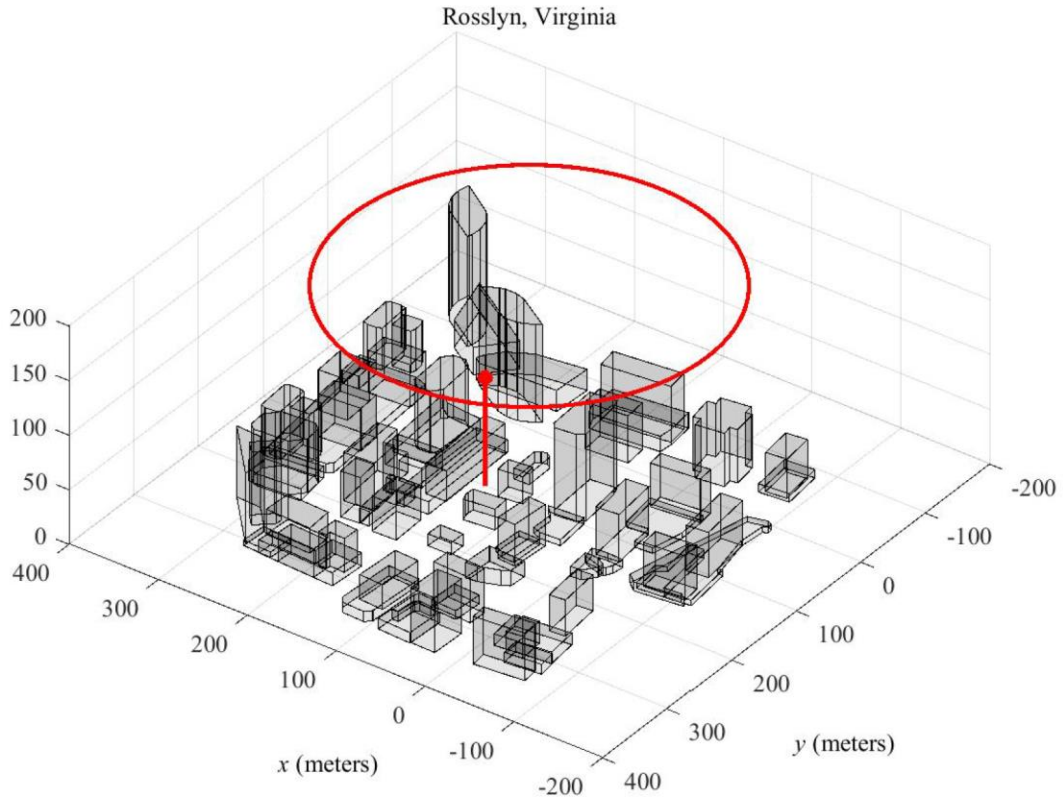

Figure 46. Circular track and the receiver; the large "thumbtack" marks the location of the street-level receiver.

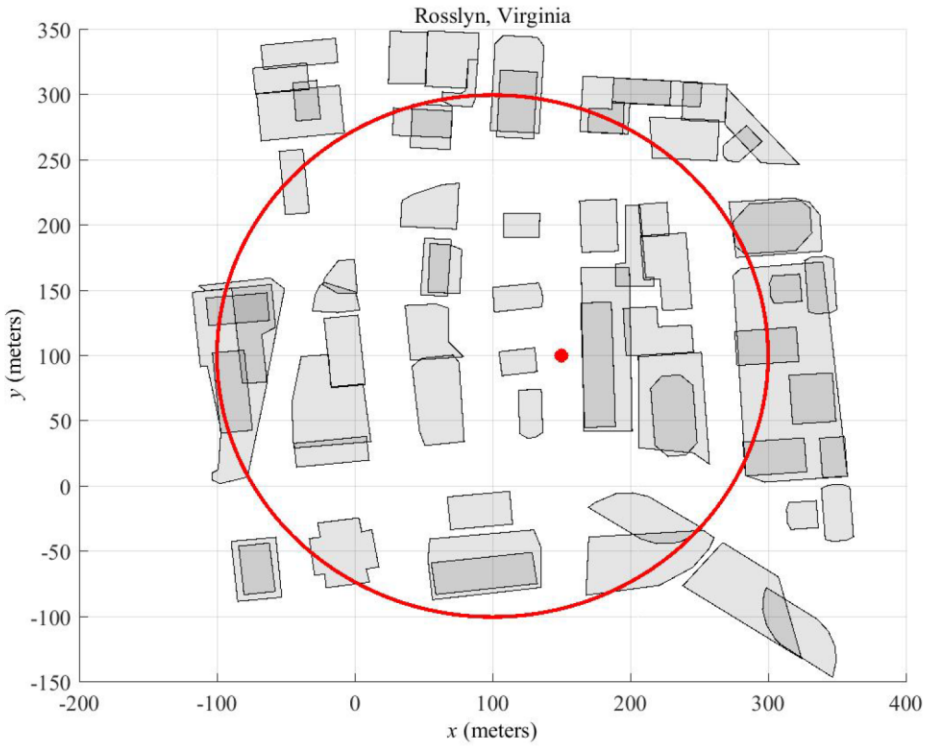

Figure 47. Top view of the circular track and the receiver.

9.2 UAV FLYING THE CIRCULAR TRACK WITH 0° ROLL

The orientation of the UAV is determined by its location along the circular track. Referring to Figure 5, the nose of the UAV or the unit vector $\widehat{\mathbf{x}}$ points along the tangent vector to the circular track, the wing or the unit vector $\widehat{\mathbf{y}}$ is horizontal, and $\widehat{\mathbf{z}}$ is the cross product of $\widehat{\mathbf{x}}$ and $\widehat{\mathbf{y}}$. Figure 48 views the cross section of the UAV's track along y-axis when the UAV has flown halfway around the circle. The vertical and horizontal antenna patterns of Figures 7 and 8 orient their spherical coordinates to this moving $\widehat{\mathbf{x}}$-$\widehat{\mathbf{y}}$-$\widehat{\mathbf{z}}$ coordinate system attached to the UAV.

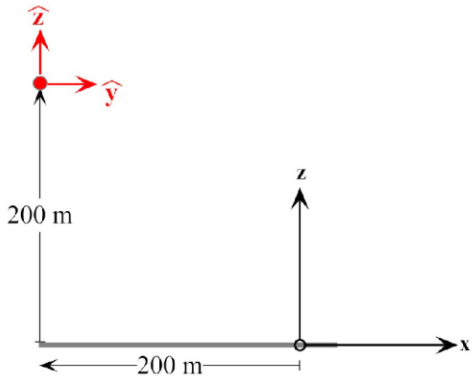

Figure 48. Vertical cross section of the circular track at azimuth $\phi = 180^\circ$ showing the UAV's orientation; $\widehat{\mathbf{x}}$ points out of the paper.

Suppressing this orientation, the channel at $f_C = 500$ MHz is the mapping

$$\phi \mapsto |h(f_C; \mathbf{r}_T(\phi), \mathbf{r}_R)|^2 \quad [\text{dB}]; \quad \mathbf{r}_R^{\mathsf{T}} = \begin{bmatrix} 150 & 100 & \end{bmatrix} \quad [\text{m}]$$

plotted in Figure 49. This circular track exhibits a deep null at $\phi = 180°$ similar to the deep null observed in the linear tracks (See Figure 23). This null provides verification that the antenna pattern is correctly integrated onto the circular track. This fading repeats everytime the UAV completes an orbit. This periodic fading provides channel knowledge to the radio system to boost throughput.

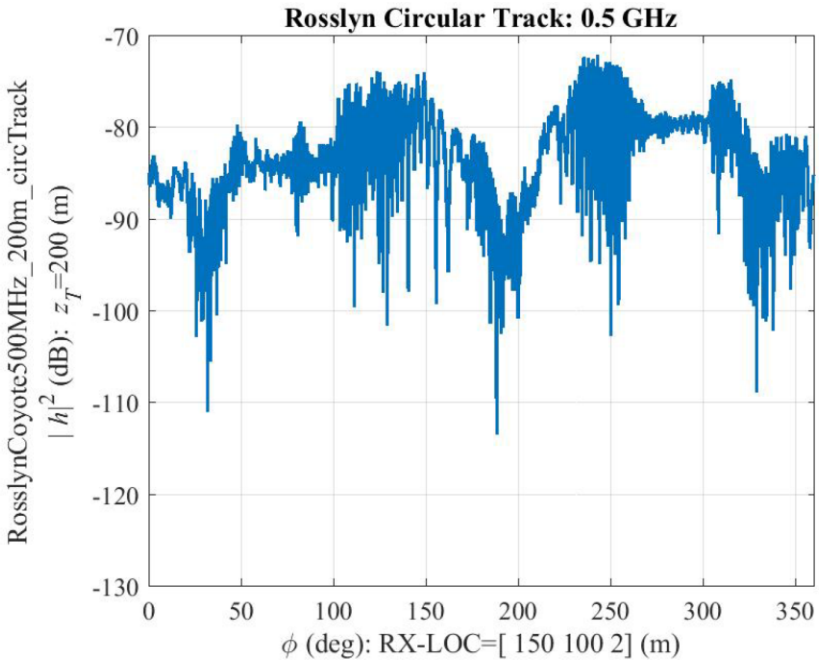

Figure 49. Channel on the circular track.

9.3 UAV FLYING THE CIRCULAR TRACK WITH $45°$ ROLL

The final simulation files the UAV flying around the circular track at constant roll of $45°$. Figure 50 shows the cross section of the UAV's track viewed along the y axis when the UAV has completed half the circle flying with a constant roll of $45°$. The vertical and horizontal antenna patterns of Figures 7 and 8 orient their spherical coordinates to this coordinate system.

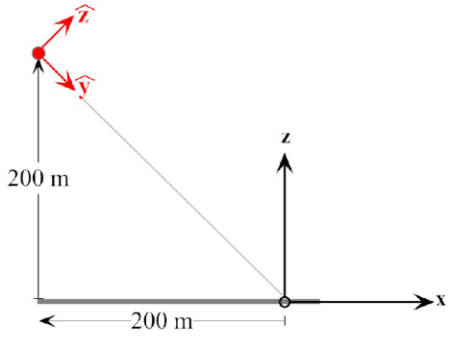

Figure 50. Vertical cross section of the circular track at azimuth $\phi = 180°$ showing the UAV flying with a constant roll of $45°$; $\hat{\mathbf{x}}$ points out of the paper.

Figure 51 shows that rolling the UAV by $45°$ boosts the channel gain over the non-rolled channel (Figure 51). When the UAV is rolled $45°$, the antenna points at the street-level receiver with zenith $\theta \approx 90°$ from the region of maximum gain. In contrast, when the UAV is flying the circular track with zero roll, the antenna points at the street-level receiver with zenith $\theta \approx 135°$ or when the gain pattern is rolling off to its null at $\theta = 180°$. This shift in the gain caused by the roll provides another verification that the antenna pattern is correctly integrated onto the circular track.

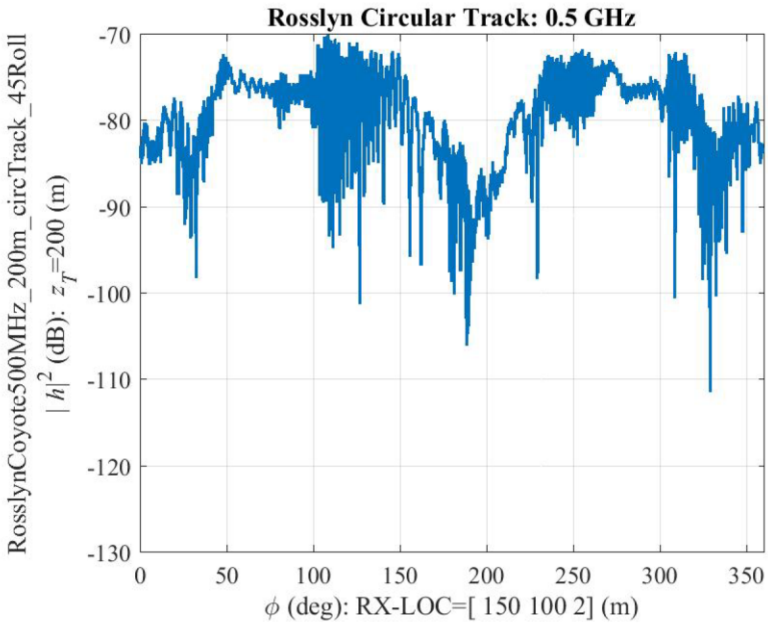

Figure 51. Channel on the circular track; UAV rolled $45°$.

9.4 CIRCULAR TRACK SUMMARY

This section focused on flying the UAV around the circular track with and without a roll. Nevertheless, some the resulting channels in Figures 49 and 51 show that:

- The UAV can increase gain by pointing the main beam into the city,
- Periodic fading on the circular track provides channel knowledge for the radio system to adapt to this orbiting UAV.

10. UAV RELAY ON A CIRCULAR TRACK

This final simulation flies the UAV around a circular track and compares the UAV relay on this track to the UAV relay over the 2-D region in Section 8. Figure 52 is a top view of the city, the circular track of the UAV, and the two nodes. As in Section 9, the circular track is 400 meters in diameter, set at 200 meters height, and centered at $x_T = 100$ and $y_T = 100$ meters. The UAV flies around this circular track with wings level or zero roll angle (See Figure 48).

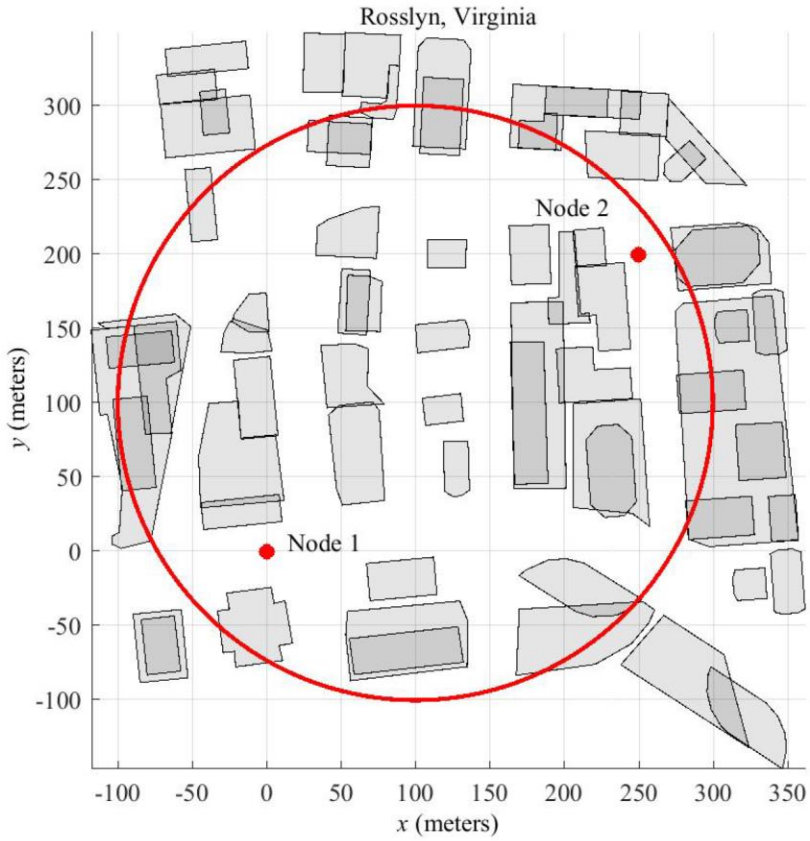

Figure 52. Top view of the circular track and the two nodes.

10.1 UAV CHANNELS ON THE CIRCULAR TRACK

Figures 53 and 54 show the UAV-to-Node channels $\{h_1(\phi)\}$ and $\{h_2(\phi)\}$. Both channels show heavy shadowing and multipath fading. Both channels show a deep null when the UAV is closest to the associated node. This null is caused by the upward pointing null of whip antenna employed by the nodes. Figure 55 shows the worst channel

$$|h_{\text{MIN}}(\phi)| = \min\{|h_2(\phi)|, |h_2(\phi)|\}$$

that determines a lower bound on the throughput of the UAV relay.

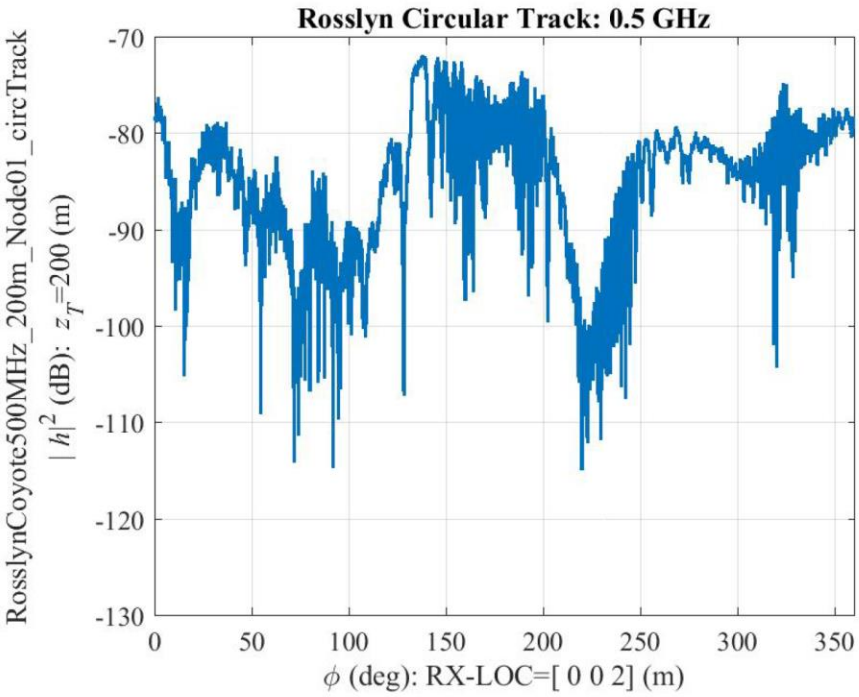

Figure 53. Channel on the circular track at Node 1.

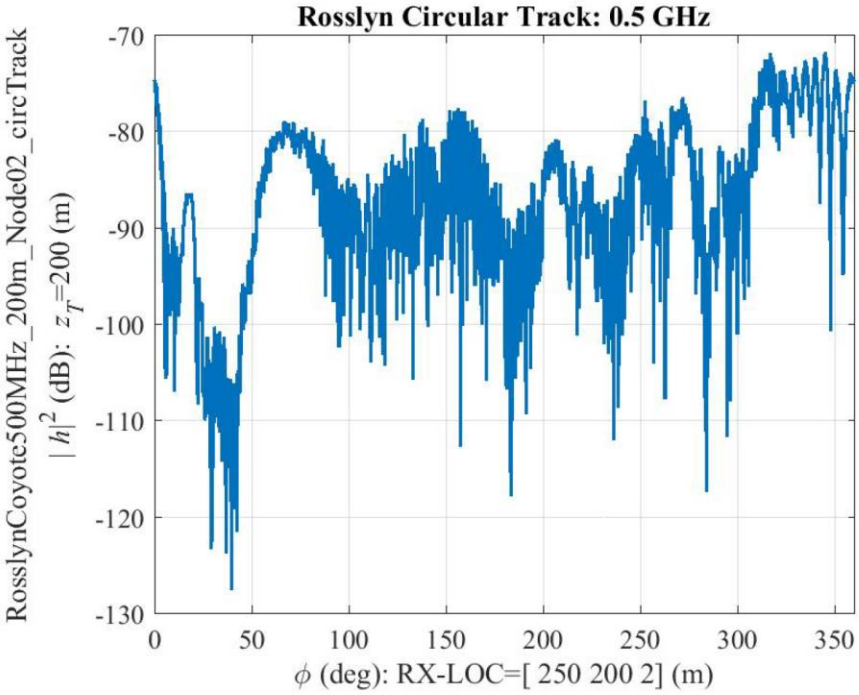

Figure 54. Channel on the circular track at Node 2.

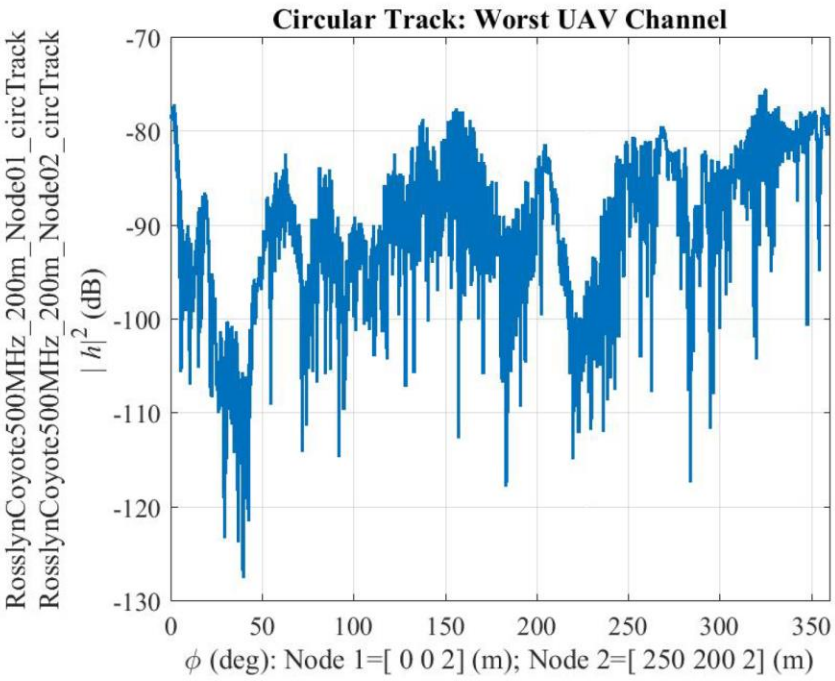

Figure 55. Worst channel relay on the circular track.

Throughput requires allocating power between the up-link and the down-link. A simple power allocation equally divides the total relay power p_Σ between the transmitting node's power p_T and the UAV's transmitting p_{UAV}:

$$p_\Sigma = p_T + p_{\text{UAV}}; \quad p_T, p_{\text{UAV}} = p_\Sigma/2.$$

The associated Shannon rate for this UAV relay—not accounting for latency—is computed at each UAV position as

$$R_b(\phi) = f_B \cdot \log_2 \left(1 + |h_{\text{MIN}}(\phi)|^2 \frac{p_\Sigma/2}{p_N} \right) \quad \text{[Mbps]},$$

where the additive noise has power $p_N = -121$ dBW. Figure 56 shows the histogram of this throughput on the circular track. The UAV relay delivers 9.1 ± 2.8 Mbps using total power $p_\Sigma = 1$ Watt. Using the same power, the ground-to-ground relay delivers only 2.1 Mbps. The tail of the histogram shows that only a small fraction of the channel perform worst than the ground-to-ground link. In terms of stealthiness, the UAV relay delivers almost five times the throughput with the ground nodes emitting half the power.

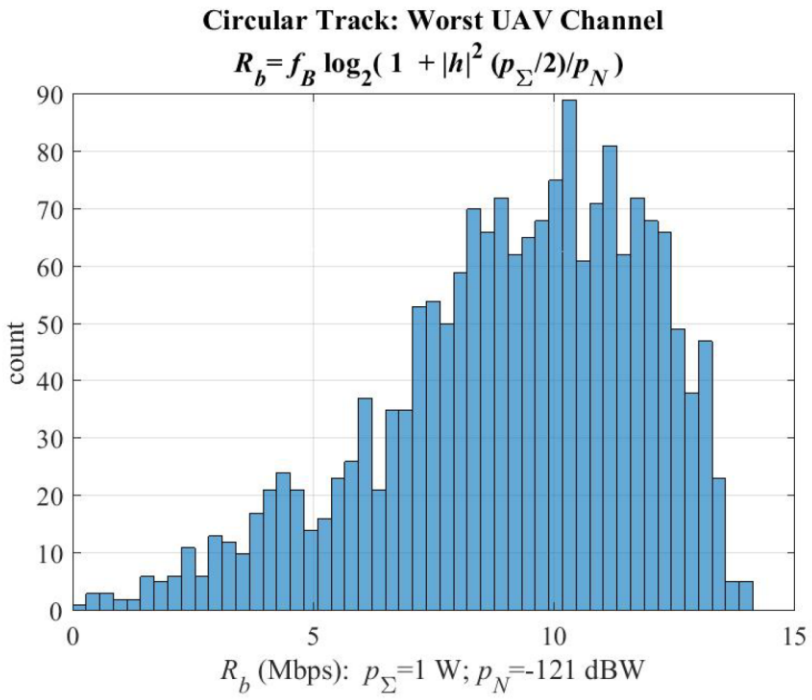

Figure 56. Histogram of the worst channel throughput on the circular track; equal-power allocation; $p_\Sigma = 1$ Watt.

10.2 SUMMARY OF THE RELAY

The circular relay (CR) track retains a "sufficient" sample of the 2-D coverage of Section 8 to deliver a statistically significant shift in throughput with less power subject to the following considerations:

CR-1 Latency is ignored.

CR-2 The channel is known.

CR-3 Equal power allocation.

Latency has a substantial effect in relay networks [15] and requires a per-packet simulation, such as the EMANE simulation [8]. The fundamental problem is wireless communication is knowing the channel. If the nodes are stationary, the channel can be "learned" after a couple of UAV orbits. Consequently, a UAV relay operating in a loitering pattern should enable high-quality channel estimation, efficient power allocation, and latency mitigation, and extensions to multiple UAVs [28], [29], [30].

11. UAV CHANNELS: SUMMARY AND RECOMMENDATIONS

These UAV simulations quantify the fading and spectra of the wireless channels interacting with mobile ground forces—assuming a 1-inch bottom-mounted whip on the UAV, half-wavelength vertical dipoles used by all ground-level nodes, and operating at 500 MHz. Even under these specific assumptions, the simulations produced the following observations repeated here for convenience:

- Both the UAV and ground antenna patterns affect the UAV loitering patterns (Section 4).
- The city's geometry, particularly building height, governs the fading extrema: heavy shadowing versus Fluctuating Two-Ray (FTR) fading (Sections 5 and 6).
- FTR fading appears as a credible model for systems employing a 1 MHz or less of bandwidth (Section 7).
- The UAV relay both increases capacity and decreases transmission power at the cost of transmitting over a spatially varying channel (Section 8, 9, 10).

These observations support both the modeling of the UAV fading for EMANE simulations and the long-term payoffs gained by understanding how the UAV antenna patterns interact with the city's "spatial filter" to generate end-to-end channels. The initial recommendations aim at the fading while the later recommendations address selecting UAV antennas to assess the performance shift of the UAV relay as a function of power and throughput.

UAV-1 Develop FTR estimators to model the multipath fading observed in to the UAV channels [22].

UAV-2 Extend Gamma fading estimators to model the heavy shadowing [4].

UAV-3 The multipath in the simulations point to employing MIMO systems on the UAV rather than single antenna systems [3].

UAV-4 The shadowing observed in the lower altitudes and the coverage plots point to simulations seeking optimal UAV loitering tracks based on city geometry (e.g., average building height and density determine UAV height).

UAV-5 The UAV relay produced substantial gains using only the simplest power control. These urban simulations are ideal for ranking wireless power control (WPC) algorithms (e.g., the WPC algorithms must contend against the time-varying channels [14]).

UAV-6 Extend these relay simulations to multiple UAV relays (e.g., UAV loitering patterns should minimize power and latency [28], [29], [30]).

UAV-7 Undertake large-scale simulations in rural scenarios [3].

UAV-8 Extend these urban simulations to model a standoff UAV conducting RF surveillance against non-cooperative wireless operations.

This page is intentionally blank.

REFERENCES

1. Abdi, A.; W. Lau; M.-S. Alouini; M. Kaveh [2003] A New Simple Model for Land Mobile Satellite Channels: First- and Second-Order Statistics, *IEEE Transactions on Wireless Communications*, 2(3).

2. Al-Ahmadi, S. [2012] Asymptotic Capacity of Opportunistic Scheduling over Gamma–Gamma (Generalised-K) Composite Fading Channels, *IET Communications*, 6(18).

3. Allen, J. C. [2014] *MIMO Channel Research*, presented at the Office of Naval Research Code 30 C4 Technical Interchange Review $\{22–24\}$-April-2014, Washington D.C.

4. Atapattu, Saman; Chintha Tellambura; Hai Jiang [2016] A Mixture Gamma Distribution to Model the SNR of Wireless Channels, *IEEE Transactions on Wireless Communications*, (ACCEPTED).

5. Bello, Philip A. [1963] Characterization of Randomly Time-Variant Linear Channels, *IEEE Transactions on Communications Systems*, CS-11, pages 360–393.

6. Daly, Michael P. [2012] *Physical-Layer Encryption Using Fixed and Reconfigurable Antennas*, Ph.D Thesis, Electrical Engineering Department, University of Illinois at Urbana-Campaign.

7. Daly, Michael P.; Ontiveros, Marcos; J. Allen; K. Buchanan, Diana Arceo [2015] Measured 2×2 MIMO UHF Channels in an Urban Environment, *2015 IEEE International Symposium on Antennas and Propagation*, July 19–25, 2015 Vancouver, BC, Canada.

8. Galgano, Steven M.; Kaushik B. Patel; Eric Schreiber [2013] *EMANE User Manual 0.8.1*, Adjacent Link LLC, 9 Kiser Lane, Bridgewater, NJ 08807.
   `Rev. 2 cs.itd.nrl.navy.mil/work/emane`

9. Garrity, Thomas A. [2015] *Electricity and Magnetism for Mathematicians*, Cambridge University Press, New York, NY.

10. Goldsmith, Adrea [2005] *Wireless Communications*, Cambridge University Press, New York, NY.

11. Gupta, Lav; Raj Jain; Gabor Vaszkun [2016] Survey of Important Issues in UAV Communication Networks, *IEEE Communications Surveys & Tutorials*, 18(2).

12. Kaiser, James F. & Ronald W. Schafer [1980] On the Use of the I_0-Sinh Window for Spectrum Analysis, *IEEE Transactions On Acoustics, Speech, And Signal Processing*, ASSP-28(1).

13. Kim, J. C. & E. I. Muehldorf [1995] *Naval Shipboard Communications Systems*, Prentice Hall, Englewood Cliffs, NJ.

14. Lauff, Sarah; Jeffery C. Allen, David F. Schwartz [2016] Wireless Power Control for Tactical MANET: Power-Rate Bounds, *Technical Report 3034*.

15. Li, Jin & Youngnam Han [2017] Optimal Resource Allocation for Packet Delay Minimization in Multi-Layer UAV Networks, *IEEE Communication Letters*, 21(3).

16. Marhefka, Ronald J. [2002] *Numerical Electromagnetics Code-Basic Scattering Code, (NEC-BSC 4.2) User's Manual*, Department of Electrical Engineering, Ohio State University, Columbus Ohio.

17. Meloling, John H. [1994] *A Caustic-Corrected Uniform Geometrical Theory of Diffractions for Evaluating High-Frequency Electro-magnetic Fields Near the Cusp of the Caustic Caused by the Curvature of an Edge*, Ph.D Thesis, The Ohio State University.

18. Mosley, Caroline [2015] Since Katrina: A Decade of NOAA Hurricane Research, *NOAA Research Communications*, National Oceanic and Atmospheric Administration.

19. Papoulis, A. [1983] *Probability, Random Variables, and Stochastic Processes*, McGraw-Hill, New York, NY.

20. Paris, J. F. [2015] Statistical Characterization of κ-ν Shadowed Fading, *IEEE Trans. Veh. Technol.*, 63(2).

21. Proakis, [1983] *Digital Communications*, third edition, McGraw-Hill Inc., New York, NY.

22. Ramirez-Espinosa, Pablo; F. Javier Lopez-Martinez; Jos F. Paris; Michel D. Yacoub; Eduardo Martos-Naya [2017] An Extension of the κ-μ Shadowed Fading Model: Statistical Characterization and Applications, `arXiv:1706.09314v1 [cs.IT]`.

23. Romero-Jerez, Juan M.; F. Javier Lopez-Martinez; José F. Paris; Andrea J. Goldsmith [2016] The Fluctuating Two-Ray Fading Model: Statistical Characterization and Performance Analysis, `1611.05063v1 [cs.IT]`.

24. Sams, Howard W. [1977] *Reference Data for Radio Engineers* (Sixth Edition), International Telephone and Telegraph Corporation.

25. Sharma, Vishal; Mehdi Bennis; Rajesh Kumar [2016] UAV-Assisted Heterogeneous Networks for Capacity Enhancement, *IEEE Communications Letters*, 20(6).

26. Sofotasios, Paschalis C. [2015] On the η-μ/gamma and the λ-μ/gamma Composite Distributions, `arXiv:1505.03978v1 [cs.IT]`.

27. Stüber, Gordon L. [2001] *Principles of Mobile Communication*, second edition, Kluwer Academic Publishers, Boston, MA.

28. Tortonesi, Mauro; Cesare Stefanelli; Erika Benvegnu; Ken Ford; Niranjan Suri; Mark Linderman [2012] Multiple-UAV Coordination and Communications in Tactical Edge networks *IEEE Communications Magazine*, 50(10).

29. Xie, Lifeng; Jie Xu; Rui Zhang [2018] Throughput Maximization for UAV-Enabled Wireless Powered Communication Networks (Invited Paper) `arXiv:1801.04545v1 [cs.IT]`.

30. Zhou, Yi; Nan Cheng; Ning Lu; Xuemin (Sherman) Shen [2015] Multi-UAV-Aided Networks, *IEEE Vehicular Technology Magazine*, 10(4).

INITIAL DISTRIBUTION

84310	Technical Library/Archives	(1)
75250	M. Daly	(1)
75250	J. Allen	(1)
71000	J. Meloling	(1)

Defense Technical Information Center
Fort Belvoir, VA 22060–6218 (1)

This page is intentionally blank.

REPORT DOCUMENTATION PAGE

Form Approved
OMB No. 0704-01-0188

PLEASE DO NOT RETURN YOUR FORM TO THE ABOVE ADDRESS.

1. REPORT DATE *(DD-MM-YYYY)*	2. REPORT TYPE	3. DATES COVERED *(From - To)*
November 2021	Final	

4. TITLE AND SUBTITLE

UAV Urban Channels Part I:
Bottom-Mounted Whip at 500 MHz.

5a. CONTRACT NUMBER

5b. GRANT NUMBER

5c. PROGRAM ELEMENT NUMBER

6. AUTHORS

Michael Daly
Jeffery Allen
John Meloling
NIWC Pacific

5d. PROJECT NUMBER

5e. TASK NUMBER

5f. WORK UNIT NUMBER

7. PERFORMING ORGANIZATION NAME(S) AND ADDRESS(ES)

NIWC Pacific
53560 Hull Street
San Diego, CA 92152–5001

8. PERFORMING ORGANIZATION REPORT NUMBER

TR 3253

9. SPONSORING/MONITORING AGENCY NAME(S) AND ADDRESS(ES)

Strategic Capabilities Office (SCO)
675 North Randolph Street
Arlington, VA 22203-2114

10. SPONSOR/MONITOR'S ACRONYM(S)

SCO

11. SPONSOR/MONITOR'S REPORT NUMBER(S)

12. DISTRIBUTION/AVAILABILITY STATEMENT

DISTRIBUTION STATEMENT A: Approved for public release. Distribution is unlimited.

13. SUPPLEMENTARY NOTES

14. ABSTRACT

This report simulates the wireless channels of a low-flying UAV relaying communications between small-unit mobile ground units operating in urban environments. The wireless channels are simulated by the *Numerical Electromagnetics Code-Basic Scattering Code* (NEC-BSC) [16]. This code approximates the 3-D electric field propagating throughout the city to user-specified accuracy. This electric field encompass the digital 3-D city, the multipath propagation, and the antenna patterns of both the UAV and the ground units. Consequently, the simulations represent wireless UAV relay channels with sufficient accuracy to assess *relative* performance shifts.

15. SUBJECT TERMS

Wireless Urban Channels; UAV Wireless Relay; Wireless UAV Performance; UAV Channel Fading; Rician Fading; Two-Ray Rician Fading, UAV Antenna Patterns; Urban RF Propagation; Multipath Propagation.

16. SECURITY CLASSIFICATION OF:			17. LIMITATION OF ABSTRACT	18. NUMBER OF PAGES	19a. NAME OF RESPONSIBLE PERSON
a. REPORT	b. ABSTRACT	c. THIS PAGE			Jeffery C. Allen
U	U	U	SAR	70	19B. TELEPHONE NUMBER *(Include area code)* (619) 553-6566

This page is intentionally blank.

This page is intentionally blank.

Naval Information Warfare Center Pacific (NIWC Pacific)
San Diego, CA 92152-5001